

SARS-CoV-2 Infects Human Engineered Heart Tissues and Models COVID-19 Myocarditis

Authors:

Adam L. Bailey^{1*}, Oleksandr Dmytrenko^{2*}, Lina Greenberg^{3*}, Andrea L. Bredemeyer², Pan Ma²,
Jing Liu², Vinay Penna², Lulu Lai², Emma S. Winkler¹, Sanja Sviben⁴, Erin Brooks⁵, Ajith P. Nair⁶,
Kent A. Heck⁷, Aniket S. Rali⁸, Leo Simpson⁶, Mehrdad Saririan⁹, Dan Hobohm⁹, W. Tom Stump³,
James A. Fitzpatrick^{4,10}, Xuping Xie¹¹, Pei-Yong Shi¹¹, J. Travis Hinson^{12,13}, Weng-Tein Gi¹⁴,
Constanze Schmidt¹⁴, Florian Leuschner¹⁴, Chieh-Yu Lin^{1,#}, Michael S. Diamond^{1,2,15,#}, Michael J.
Greenberg^{3,#}, Kory J. Lavine^{1,2,16,#}

*Co-first authors

#Co-senior authors

Affiliations:

¹Department of Pathology and Immunology, Washington University School of Medicine, St. Louis, MO, USA

²Department of Medicine, Washington University School of Medicine, St. Louis, MO, USA

³Department of Biochemistry and Molecular Biophysics, Washington University School of Medicine, St. Louis, MO, USA

⁴Washington University Center for Cellular Imaging, Washington University School of Medicine, St. Louis, MO, USA

⁵Department of Pathology & Laboratory Medicine, University of Wisconsin Hospital and Clinics, Madison, Wisconsin, USA

⁶Department of Medicine, Baylor College of Medicine, Houston, Texas, USA

⁷Department of Pathology, Baylor College of Medicine, Houston, Texas, USA

⁸Department of Medicine, Vanderbilt University, Nashville, Tennessee, USA

⁹Valleywise Health/Creighton University, Phoenix, AZ, USA

¹⁰Departments of Neuroscience, Cell Biology & Physiology, and Biomedical Engineering, Washington University School of Medicine, St. Louis, MO, USA

¹¹Department of Biochemistry and Molecular Biology, University of Texas Medical Branch, Galveston, TX, USA

¹²Departments of Cardiology and Genetics and Genome Sciences, UConn Health, Farmington, CT.

¹³The Jackson Laboratory for Genomic Medicine, Farmington, CT

¹⁴Department of Internal Medicine III, University Hospital Heidelberg, University of Heidelberg, Heidelberg, Germany

¹⁵Department of Molecular Microbiology, Washington University School of Medicine, St. Louis, MO, USA

¹⁶Department of Developmental Biology, Washington University School of Medicine, St. Louis, MO, USA

Keywords: SARS-CoV-2, COVID-19, Myocarditis, Engineered Heart Tissue, Cardiomyocyte, Macrophage

45
46
47
48
49
50
51
52
53
54
55
56
57
58
59
60
61
62
63
64
65
66
67
68
69
70
71

Running Title: SARS-CoV-2 Infects Human Cardiomyocytes

Corresponding authors information:

Kory J. Lavine, MD, PhD
660 South Euclid Campus Box 8086
St. Louis, MO, 63110
Phone: 314 362-1171
Fax: 314 362-0186
Email: klavine@wustl.edu

Michael J. Greenberg, PhD
660 South Euclid Campus Box 8231
St. Louis, MO, 63110
Phone: 314 362-8670
Fax: 314 362-7183
Email: greenberg@wustl.edu

Michael S. Diamond, MD, PhD
660 South Euclid Campus Box 8051
Phone: 314 362-2842
Fax: 314 362-9230
Email: diamond@wusm.wustl.edu

72 **Abstract:**

73

74 Epidemiological studies of the COVID-19 pandemic have revealed evidence of cardiac
75 involvement and documented that myocardial injury and myocarditis are predictors of poor
76 outcomes. Nonetheless, little is understood regarding SARS-CoV-2 tropism within the heart and
77 whether cardiac complications result directly from myocardial infection. Here, we develop a
78 human engineered heart tissue model and demonstrate that SARS-CoV-2 selectively infects
79 cardiomyocytes. Viral infection is dependent on expression of angiotensin-I converting enzyme 2
80 (ACE2) and endosomal cysteine proteases, suggesting an endosomal mechanism of cell entry.
81 After infection with SARS-CoV-2, engineered tissues display typical features of myocarditis,
82 including cardiomyocyte cell death, impaired cardiac contractility, and innate immune cell
83 activation. Consistent with these findings, autopsy tissue obtained from individuals with COVID-
84 19 myocarditis demonstrated cardiomyocyte infection, cell death, and macrophage-predominate
85 immune cell infiltrate. These findings establish human cardiomyocyte tropism for SARS-CoV-2
86 and provide an experimental platform for interrogating and mitigating cardiac complications of
87 COVID-19.

88 **Introduction:**

89 Severe Acute Respiratory Syndrome Coronavirus 2 (SARS-CoV-2) is the cause of the
90 ongoing Coronavirus Disease-2019 (COVID-19) pandemic. Since its emergence in Wuhan, China
91 in late 2019, SARS-CoV-2 has infected millions of people worldwide, overwhelmed the capacity
92 of healthcare systems, and continues to result in unacceptably high mortality rates. Although most
93 severe cases of COVID-19 are characterized by respiratory distress, the disease has a highly
94 variable clinical course with myriad manifestations. Epidemiological studies have identified pre-
95 existing cardiovascular disease as a strong risk factor for the development of severe COVID-19
96 and mortality (reviewed in¹). Cardiovascular manifestations of COVID-19 including elevated
97 troponin, reduced left ventricular systolic function, and arrhythmias are consistent with
98 cardiomyocyte injury. Cardiac complications occur in 20-44% of hospitalized patients, and
99 constitute an independent risk factor for COVID-19 mortality¹⁻⁴. Cardiac MRI studies have
100 suggested that persistent myocardial injury may be more common than appreciated and occur in
101 less severe forms of COVID-19⁵⁻⁷. The mechanistic basis by which SARS-CoV-2 results in
102 cardiac dysfunction remains obscure. It remains unknown whether these effects are a result of
103 direct viral infection of cardiac cells or a systemic inflammatory response to extracardiac
104 infection⁸. If direct infection does contribute to COVID-19-associated cardiac injury, defining the
105 cell-types susceptible to infection will be important for understanding COVID-19 cardiac
106 pathogenesis and devising effective treatment strategies.

107 It has been challenging to study the cardiac manifestations of COVID-19. Obtaining
108 cardiac tissue from critically ill patients with suspected COVID-19 myocarditis poses unique
109 challenges. Furthermore, there are few animal models to study cardiovascular complications
110 observed in SARS-CoV-2 infected humans⁹. The most commonly used laboratory animal model,
111 the mouse, is not susceptible to SARS-CoV-2 infection due to poor affinity of the viral spike protein
112 for the murine ACE2 receptor^{10,11}, and systems that enable expression of human ACE2 from cells
113 in the murine cardiovascular system are not yet widely available. Therefore, there is a critical need

114 to develop robust model systems that enable the investigation of the cardiovascular complications
115 of COVID-19.

116 Human engineered heart tissues (EHTs) provide unique advantages as model systems
117 for studying COVID-19 cardiac pathology. EHTs are self-assembled using defined cellular and
118 extracellular matrix compositions. EHTs generate contractile force, display electrical coupling,
119 and have cellular organization that mimics myocardial tissue (reviewed in^{12,13}). Human EHTs can
120 be formed from human pluripotent stem cell (hPSC)-derived cardiomyocytes, where the three-
121 dimensional environment of the EHT promotes the maturation of these cells¹⁴.

122 Here, we devised an EHT model of COVID-19 myocarditis and tested the hypothesis that
123 SARS-CoV-2 promotes cardiac pathology by infecting cardiomyocytes and activating local
124 immune responses. We demonstrate that SARS-CoV-2 selectively infects and replicates within
125 hPSC-derived cardiomyocytes, ultimately resulting in cardiomyocyte cell death. We provide
126 evidence that cardiomyocyte infection is dependent on ACE2 expression and endosomal cysteine
127 protease activity. SARS-CoV-2-infected EHTs displayed typical features of myocarditis, including
128 activation of immune cells, decreased contractile force generation, and cardiomyocyte cell death.
129 Furthermore, autopsy and biopsy samples from four patients with confirmed SARS-CoV-2
130 infection and clinical myocarditis demonstrated patchy cardiomyocyte infection that was
131 accompanied by myocardial cell death and macrophage accumulation. These findings
132 demonstrate that SARS-CoV-2 can productively infect human cardiomyocytes and establish
133 EHTs as a platform for mechanistic investigation of COVID-19 myocarditis.

134 **Results:**

135 **ACE2 is expressed in human cardiomyocytes**

136 To explore whether human cardiomyocytes might be susceptible to SARS-CoV-2
137 infection, we examined the expression of angiotensin converting enzyme 2 (ACE2) within the
138 human heart. Previous studies have established that ACE2 serves as a cell-surface receptor for
139 SARS-CoV-2 through interactions with the spike protein in numerous human cell types^{15,16}.
140 Immunostaining of human left ventricular myocardial tissue revealed evidence of ACE2
141 expression in cardiomyocytes (**Fig. 1a**). We observed significant variation in ACE2 expression
142 between individual cardiomyocytes within the same myocardial specimen. ACE2 mRNA was
143 abundantly expressed in the healthy human heart and further increased in the context of chronic
144 heart failure (**Fig. 1b**). RNA sequencing of human pediatric and adult heart failure specimens
145 revealed robust expression of ACE2 mRNA within the human heart across the spectrum of age
146 (**Fig. 1c**). Consistent with our immunostaining findings, primary human cardiomyocytes obtained
147 from the left ventricle and atria expressed ACE2 mRNA (**Fig. 1d**). These data are consistent with
148 prior single cell and bulk RNA sequencing analyses of human myocardium and suggest that
149 cardiomyocytes might be permissive to SARS-CoV-2 infection¹⁷.

150 To ascertain whether human pluripotent stem cell-derived cardiomyocytes (hPSC-derived
151 CMs) can serve as an appropriate model to study cardiac SARS-CoV-2 infection, we measured
152 ACE2 mRNA expression in hPSC-derived CMs. Quantitative RT-PCR revealed that hPSC-
153 derived CMs abundantly expressed ACE2 mRNA. In contrast, minimal ACE2 mRNA was detected
154 in human dermal fibroblasts, hPSC-derived cardiac fibroblasts, or human fetal cord blood derived-
155 macrophages (**Fig. S1a-c**). Human engineered heart tissues (EHTs) self-assembled between two
156 deformable polydimethylsiloxane (PDMS) posts after mixing cells in an extracellular matrix
157 composed of collagen and matrigel (**Fig. S1d**). EHTs composed of either hPSC-derived CMs and
158 fibroblasts or hPSC-derived CMs, fibroblasts, and macrophages also expressed ACE2 mRNA
159 (**Fig. S1e**). Immunostaining of EHTs confirmed the presence of ACE2 protein specifically in

160 hPSC-derived CMs (**Fig. S1f**). These data suggest that hPSC-derived CMs might be susceptible
161 to SARS-CoV-2 infection and serve as a suitable experimental model to study cardiac
162 manifestations of COVID-19.

163

164 **SARS-CoV-2 infects hPSC-derived cardiomyocytes**

165 To determine the susceptibility of different myocardial cell types to SARS-CoV-2 infection,
166 we inoculated various stromal populations with a recombinant SARS-CoV-2 clone containing a
167 NeonGreen fluorescent reporter (SARS-CoV-2-mNeonGreen)¹⁸. NeonGreen is expressed from a
168 viral subgenomic RNA, indicative of active viral replication. We were unable to detect infection of
169 primary human cardiac fibroblasts, endothelial cells, or macrophages (**Fig. 1e**, gating schemes:
170 **Fig. S2**). hPSC-derived endothelial cells and cardiac fibroblasts were also not susceptible to
171 infection (**Fig. S1g**). In contrast, two independent lines of hPSC-derived cardiomyocytes (hPSC-
172 derived CMs) were permissive to SARS-CoV-2 infection (**Fig. 1f**). Undifferentiated hPSC lines did
173 not demonstrate evidence of infection (**Fig S3**).

174 To confirm cardiomyocyte tropism, we inoculated various combinations of hPSC-derived
175 CMs, fibroblasts, and macrophages grown in monolayer culture with wild-type SARS-CoV-2
176 (USA_WA1/2019). We analyzed tissue culture supernatants for production of infectious virus
177 using a Vero cell infection-based focus forming assay, and we measured intracellular viral RNA
178 transcript levels using RT-qPCR at 3 days post-inoculation. These assays revealed the production
179 of infectious virus (**Fig. 2a**) and viral RNA (**Fig. 2b**) selectively in cultures that contained hPSC-
180 derived CMs. Cultures lacking hPSC-derived CMs contained viral loads that were equivalent to
181 media-only controls. A time course of hPSC-derived CM infection showed that cardiomyocytes
182 rapidly produced infectious virus with peak titers observed at day 3 post-inoculation. These
183 kinetics were closely mirrored by SARS-CoV-2-mNeonGreen (**Fig. 2c**).

184 Using SARS-CoV-2-mNeonGreen, we examined the relationship between viral replication
185 and cell death using flow cytometry. Although the percentage of hPSC-derived CMs that were

186 mNeonGreen-positive peaked at day 3 post-inoculation, significant levels of hPSC-derived CM
187 cell death were not observed until 4-5 days post-inoculation (**Fig. 2d**) indicating that viral infection
188 precedes hPSC-derived CM cell death. SARS-CoV-2-infected cardiomyocytes also displayed
189 characteristics of cytopathic effects. Cellular rounding, clumping, and syncytium formation first
190 were observed on day 3 post-inoculation. Distortion of cellular morphology was evident by day 4
191 post-inoculation and cultures contained largely dead cells and debris by days 5-6 post-inoculation
192 (**Fig. 2e**).

193 To verify that cardiomyocytes are the primary target of SARS-CoV-2 in a simulated cardiac
194 environment, we infected two-dimensional tissues assembled with hPSC-derived CMs (80%),
195 fibroblasts (10%), and macrophages (10%) with SARS-CoV-2-mNeonGreen. Flow cytometry
196 performed 3 days following infection revealed mNeonGreen expression only in CD90⁻CD14⁻
197 TNNT2⁺ cardiomyocytes. mNeonGreen was not detected in CD90⁺ fibroblasts or CD14⁺
198 macrophages within infected two-dimensional tissues (**Fig. 2f-g, Fig. S4**). These data
199 demonstrate selective viral tropism in cardiomyocytes. Consistent with this conclusion,
200 transmission electron microscopy of infected two-dimensional tissues performed 3 days post-
201 inoculation demonstrated the presence of coronavirus particles within infected hPSC-derived
202 CMs. Micrographs revealed structural features of coronaviruses including the presence of a tri-
203 laminar envelope and characteristic cross-sections through the nucleocapsid^{19,20} (**Fig. 2h**). Virions
204 were identified within perinuclear endosomal-like structures of hPSC-derived CMs. We observed
205 various stages of virion assembly including budding from intracellular membranes. Virions were
206 not detected in mock-infected cardiomyocytes.

207

208 **RNA sequencing identified robust viral transcription and the activation of innate immune** 209 **responses in hPSC-derived cardiomyocytes and two-dimensional tissues**

210 To examine viral transcription and the host immune response to SARS-CoV-2 infection,
211 we performed RNA sequencing. Cultures containing either hPSC-derived CMs, fibroblasts, or

212 macrophages were either mock-infected or inoculated with SARS-CoV-2. We also examined two-
213 dimensional co-culture tissues assembled with 80% cardiomyocytes, 10% fibroblasts, and 10%
214 macrophages. Cells and tissues were harvested on day 3 post-inoculation. Principal component
215 analysis revealed separation between experimental groups consistent with their distinct cellular
216 composition (**Fig. 3a**). Classification of transcript types demonstrated that infected hPSC-derived
217 CMs and two-dimensional tissues comprised of hPSC-derived CMs and fibroblasts or hPSC-
218 derived CMs, fibroblasts, and macrophages contained abundant viral transcripts (**Fig. S5a**). We
219 then assessed the expression of specific viral transcripts by aligning the RNA sequencing data to
220 the SARS-CoV-2 genome and transcriptome. Subgenomic RNAs were identified based on the
221 presence of 5' leader sequences²¹. We observed robust expression of most SARS-CoV-2
222 genomic and subgenomic RNAs in infected hPSC-derived CMs and two-dimensional tissues with
223 the exception of ORF7b (**Fig. 3b, Fig. S5b**).

224 To facilitate differential expression analysis of host genes, we censored viral RNAs from
225 the RNA sequencing computational model. This was necessary given the asymmetric prevalence
226 of viral transcripts across samples. We identified numerous host genes that were differentially
227 regulated upon SARS-CoV-2 infection in each of the examined cell types and two-dimensional
228 tissues (**Fig. 3c**). Conditions that supported viral replication (hPSC-derived CMs and two-
229 dimensional tissues) displayed the greatest overlap in differentially expressed genes. Cell types
230 that did not support viral replication (fibroblasts and macrophages) also demonstrated numerous
231 differentially expressed host genes, indicating that SARS-CoV-2 might elicit changes in host gene
232 expression in the absence of direct viral infection. Notably, host genes differentially expressed in
233 fibroblasts and macrophages exposed to SARS-CoV-2 were largely distinct (**Fig. 3d**). These
234 findings suggest that elements within or on the surface of SARS-CoV-2 virions may serve as
235 pathogen-associated molecular patterns (PAMPs) and stimulate distinct gene expression
236 programs in differing cell types.

237 GO pathway analysis revealed that infected hPSC-derived CMs and two-dimensional co-
238 culture tissues showed upregulation of genes associated with immune cell activation, stress-
239 induced transcription, and responses to pathogens including viruses. Genes associated with
240 metabolism, oxidative phosphorylation, and mitochondrial function were downregulated by
241 infection. Two-dimensional tissues displayed alterations in other pathways including upregulation
242 of cellular responses to cytokines and downregulation of genes involved in muscle contraction
243 (**Fig. 3e-f**). Host genes differentially expressed in macrophages and fibroblasts were associated
244 with pathways involved in innate immune cell activation, migration, and cytokine responses (**Fig.**
245 **3g-h**).

246 Examination of specific genes differentially regulated in infected hPSC-derived CMs and
247 two-dimensional tissues (**Fig. 3i**) revealed marked reduction in components of the electron
248 transport chain (ATP synthase, mitochondrial cytochrome C oxidase, NADPH dehydrogenase)
249 and key upstream metabolic regulators (glycerol-3-phosphate dehydrogenase, pyruvate
250 dehydrogenase, succinate dehydrogenase complex). *PDK4*, an inhibitor of pyruvate
251 dehydrogenase was upregulated in infected hPSC-derived CMs and two-dimensional tissues. We
252 also observed marked downregulation of numerous components and regulators of the contractile
253 apparatus including cardiac actin, troponin subunits, myosin light and heavy chains, desmin,
254 phospholamban, and calsequestrin in infected two-dimensional tissues. Infected hPSC-derived
255 CMs displayed similar changes, albeit to a lesser extent. *ACE2* expression was diminished in
256 infected cardiomyocytes and two-dimensional tissues.

257 Infected hPSC-derived CMs and two-dimensional tissues also displayed upregulation of
258 key regulators of innate immunity (**Fig. 3i**). Type I interferon (IFN) activation was apparent by the
259 increased expression of *IFNB1* and numerous IFN stimulated genes including *IFIT1*, *IFIT2*, *IFIT3*,
260 *ISG15*, *MX1*, and *OAS1*. Stress response programs (FOS) and cytokine expression (TNF) were
261 similarly upregulated in these cell types. Consistent with a greater innate immune response in
262 two-dimensional tissues, we found that several chemokines (*CCL3*, *CCL4*, *CCL7*, *CCL8*, and

263 *CXCL8*) and cytokines (*IL1B*, *IL6*, and *CSF3*) were selectively upregulated in infected two-
264 dimensional tissues. Macrophages and fibroblasts contributed to enhanced chemokine and
265 cytokine responses in two-dimensional tissues. *CCL3*, *CCL4*, and *CCL8* were selectively
266 expressed in infected macrophages and *CSF3*, *CXCL8*, *IL1B*, and *IL6* were induced in infected
267 fibroblasts (**Fig. S5c**).

268

269 **SARS-CoV-2 entry into hPSC-derived cardiomyocytes is mediated by ACE2 and** 270 **endosomal cysteine proteases**

271 To elucidate the mechanism(s) by which SARS-CoV-2 enters cardiomyocytes, we
272 examined SARS-CoV-2 infection of hPSC-derived CMs in the presence of well-established entry
273 inhibitors. ACE2 serves as the cell-surface receptor for SARS-CoV-2 in humans^{15,16}. Blockade of
274 ACE2 with anti-hACE2 antibody abrogated SARS-CoV-2-NeonGreen infectivity in hPSC-derived
275 CMs as measured by NeonGreen-positivity and viral RNA extracted from the supernatant of
276 infected cultures. The extent of blockade was comparable to treatment with remdesivir, a potent
277 inhibitor of the SARS-CoV-2 RNA-dependent RNA polymerase²²⁻²⁴ (**Fig. 4a-b**).

278 After binding to ACE2, the SARS-CoV (and SARS-CoV-2) spike protein must undergo
279 proteolytic activation to initiate membrane fusion²⁵. Host proteases located at the plasma
280 membrane (TMPRSS2) or within endosomes (cathepsins) most commonly perform this function.
281 The relative contributions of each of these protease families to SARS-CoV-2 infection varies by
282 cell-type^{15,25}. RNA sequencing data revealed that hPSC-derived CMs express robust levels of
283 ACE2 and multiple endosomal proteases including cathepsins and calpains (**Fig. 4c**). ACE2
284 mRNA was not abundantly expressed in either macrophages or fibroblasts. While TMPRSS2
285 expression was present at the lower limit of detection for RNAseq, we detected low, but
286 measurable levels of TMPRSS2 by RT-qPCR in hPSC-derived CMs, but not in fibroblasts or
287 macrophages (**Fig. 4c-d**).

288 To determine whether SARS-CoV-2 enters cardiomyocytes through an endosomal or
289 plasma membrane route, we inoculated hPSC-derived CMs with SARS-CoV-2-mNeonGreen and
290 administered either the endosomal cysteine protease inhibitor E-64, which blocks cathepsins, or
291 the serine protease inhibitor camostat mesylate, which blocks TMPRSS2 (and possibly
292 TMPRSS4)²⁵. Notably, E-64 abolished SARS-CoV-2 infection of hPSC-derived CMs as
293 demonstrated by reduced mNeonGreen expression and viral RNA within the supernatant (**Fig.**
294 **4e-f**). In contrast, camostat had no effect on cardiomyocyte infection over a range of doses (**Fig.**
295 **4g-h**). Thus, SARS-CoV-2 enters cardiomyocytes through an endosomal pathway that requires
296 cathepsin but not TMPRSS2-mediated cleavage.

297

298 **EHTs model COVID-19 myocarditis**

299 Myocarditis is characterized by direct viral infection of cardiomyocytes and accumulation
300 of immune cells at sites of active infection or tissue injury^{26,27}. To examine whether SARS-CoV-2
301 infection of cardiomyocytes in a three-dimensional environment mimics aspects of viral
302 myocarditis, we generated EHTs containing either hPSC-derived CMs and fibroblasts or hPSC-
303 derived CMs, fibroblasts, and macrophages. EHTs were seeded in a collagen-Matrigel matrix
304 between two PDMS posts, infected with SARS-CoV-2, and harvested 5 days after inoculation.
305 Hematoxylin and eosin (H&E) staining revealed evidence of tissue injury and increased interstitial
306 cell abundance within the periphery of SARS-CoV-2-infected EHTs (**Fig. 5a**). Immunostaining for
307 the viral nucleocapsid protein demonstrated evidence of prominent infection at the periphery of
308 the EHT. Nucleocapsid staining was localized within hPSC-derived CMs. Staining for CD68
309 demonstrated macrophage accumulation corresponding to sites of interstitial cell accumulation
310 and viral infection (**Fig. 5b, Fig. S6**). Enrichment of nucleocapsid staining at the periphery of the
311 tissue suggests that viral diffusion might be limited by the three-dimensional EHT environment.
312 Consistent with our immunostaining results, infected EHTs (with and without macrophages)
313 accumulated high levels of viral RNA, as detected by quantitative RT-PCR (**Fig. 5c**). *In situ*

314 hybridization for viral spike sense and antisense RNA was also indicative of viral replication within
315 EHTs (**Fig. 5d, Fig. S7**).

316

317 **SARS-CoV-2 infection causes contractile dysfunction and cell death**

318 Reduced left ventricular systolic function has been reported in severe cases of COVID-19
319 myocarditis²⁸. Therefore, we examined the effect of SARS-CoV-2 infection on cardiomyocyte
320 contractile function in EHTs. EHTs were seeded between two deformable PDMS posts of known
321 stiffness. As the tissue contracts, it displaces the posts, and by tracking the displacement of the
322 posts as a function of time, we calculated the speed of contraction and relaxation. The average
323 peak displacement was calculated for each spontaneously contracting tissue over the course of
324 at least 60 seconds (**Supplemental Movies 1-2**).

325 EHTs consisting of hPSC-derived CMs and fibroblasts were assembled and allowed to
326 mature for 7 days prior to infection. EHTs were inoculated with SARS-CoV-2, and contractile
327 function was analyzed daily. From days 0 to 3 post infection, the average maximal displacement
328 generated during beating did not differ between the mock and SARS-CoV-2-infected tissues.
329 However, on days 4 to 5 post infection, the SARS-CoV-2 inoculated tissues showed reduced
330 contraction relative to the mock-infected tissues (**Fig. 5e-f**). On day 5 after inoculation, the
331 maximal displacement produced during contraction by the SARS-CoV-2 inoculated tissues was
332 markedly lower than mock infected-tissues. Moreover, the tissues show reduced speed of
333 contraction and relaxation, consistent with systolic dysfunction (**Fig. 5g**).

334

335 **Mechanisms of reduced EHT contractility**

336 To examine whether cardiomyocyte cell death might serve as a mechanism explaining
337 reduced EHT contractility on days 4 to 5 post inoculation, we performed TUNEL staining.
338 Consistent with the temporal course of SARS-CoV-2 cardiomyocyte infection and cell death in
339 our two-dimensional hPSC-CM cultures (**Fig. 2d**), we observed increased numbers of TUNEL

340 positive cardiomyocytes in SARS-CoV-2 infected EHTs on day 5 post infection (**Fig. 6a-b**). Our
341 RNA sequencing data suggest that other mechanisms also may contribute to reduced EHT
342 contractility, including decreased expression of genes important for sarcomere function and
343 metabolism as well as activation of host immune responses (**Fig. 3i**). Consistent with the
344 possibility that disrupted sarcomere gene expression might contribute to reduced EHT
345 contractility, immunostaining of hPSC-derived CMs infected with SARS-CoV-2 revealed evidence
346 of sarcomere loss 3 days following infection (**Fig. 6c**), a time point that preceded cell death.
347 Furthermore, immunostaining of EHTs demonstrated loss of Troponin T expression in infected
348 cardiomyocytes. (**Fig. 6d-e**). Thus, the reduction in contractile function may be multifactorial with
349 contributions from virus-induced cardiomyocyte cell death and loss of sarcomere elements.

350 We then examined the mechanistic relationship between cardiomyocyte infection,
351 inflammatory signaling, sarcomere breakdown, and cell death. Inhibition of viral entry (ACE2
352 neutralizing antibody) or viral replication (remdesivir) was sufficient to prevent type I IFN and TNF
353 expression following SARS-CoV-2 infection (**Fig. 6f-g**). Remdesivir similarly reduced
354 inflammatory gene expression in 3D EHTs (**Fig. S8a-b**). These data establish that viral infection
355 represents the upstream driver of inflammation in our model system.

356 To examine the impact of cardiomyocyte inflammatory signaling on cardiomyocyte cell
357 death, sarcomere gene expression, and sarcomere structure, we focused on inhibiting viral
358 nucleic acid sensing. TBK1 (TANK-binding kinase 1) is an essential mediator of numerous nucleic
359 acid sensing pathways including RIG-I, MAVS, STING, and TLRs^{29,30}. Inhibition of TBK1 activity
360 was sufficient to reduce type I IFN activity (primary inflammatory signature identified in infected
361 cardiomyocytes, **Fig 3i**) without impacting viral load or cardiomyocyte infectivity (**Fig. 6f-h**).
362 Inhibition of TBK1 activity during SARS-CoV-2 cardiomyocyte infection had no impact on
363 cardiomyocyte cell death (**Fig. 6i**). While TBK1 inhibition prevented reductions in TNNT2 and
364 MYH7 mRNA expression following cardiomyocyte SARS-CoV-2 infection, sarcomere breakdown
365 remained prevalent in infected cardiomyocytes treated with the TBK1 inhibitor. In contrast,

366 remdesivir prevented both reductions in TNNT2 and MYH7 mRNA expression and sarcomere
367 loss following SARS-CoV-2 infection (**Fig. 6j-k, Fig. S8c-d**). These data indicate that SARS-CoV-
368 2 elicits an inflammatory response in cardiomyocytes that is at least partially dependent on viral
369 nucleic acid sensing and TBK1 signaling. However, TBK1-dependent cardiomyocyte
370 inflammation does not appear responsible for sarcomeric disassembly or cardiomyocyte cell
371 death. These findings do not rule out the possibility that other inflammatory pathways or cross-
372 talk between infected cardiomyocytes and immune cells contributes to reduced EHT contractility.
373

374 **Evidence of cardiomyocyte infection in COVID-19 myocarditis**

375 To validate the myocarditis phenotype generated by SARS-CoV-2 infection of the EHT
376 model, we obtained autopsy and endomyocardial biopsy specimens from four subjects with
377 confirmed SARS-CoV-2 infection and clinical diagnoses of myocarditis. Evidence of myocardial
378 injury (elevated troponin) and left ventricular systolic dysfunction were present in each case
379 (**Table 1**). Coronary angiography demonstrated no evidence of luminal stenosis or thrombosis.
380 The presence of SARS-CoV-2 RNA from nasopharyngeal samples was confirmed by clinical
381 diagnostic testing or post-mortem.

382 Postmortem microscopic examination of the left ventricular myocardium demonstrated
383 areas of cardiomyocyte necrosis and degenerative vacuolization of cardiomyocyte cytoplasm
384 were noted accompanied by a mixed mononuclear cell infiltrate (**Fig. 7a**). These changes are
385 distinct from postmortem autolytic changes. Examination of the coronary arteries from the COVID-
386 19 myocarditis autopsy cases demonstrated non-obstructive mild atherosclerotic changes,
387 consistent with the angiogram findings. There was no evidence of microvascular injury or
388 thromboembolic events. Two autopsy heart samples from subjects with metastatic carcinoma and
389 an inherited neurodegenerative disease with similar tissue procurement times were included as
390 negative controls.

391 RNA *in situ* hybridization for SARS-CoV-2 spike and nucleocapsid genes revealed
392 evidence of viral RNA within the myocardium of each COVID-19 myocarditis subject. Viral
393 transcripts were located in cytoplasmic and perinuclear locations within cells that were
394 morphologically consistent with cardiomyocytes (**Fig. 7b, Fig. S9a-b**). Viral transcripts also were
395 identified in airway epithelial cells within the lung of this subject and other myocardial cell types
396 including perivascular adipocytes and pericytes (**Fig. S9c**). Immunostaining for the nucleocapsid
397 protein further demonstrated presence of viral protein in cardiomyocytes **Fig. 7c**). The COVID-19
398 myocarditis immune cell infiltrate was characterized by accumulation of a mixed population of
399 CCR2⁻ and CCR2⁺ macrophages within injured areas of the myocardium (**Fig. 7d**). Minimal
400 evidence of T-cell infiltration was noted (**Fig. 7e**). Macrophage abundance was highest in areas
401 that demonstrated evidence of cardiomyocyte injury as depicted by complement deposition (C4d
402 staining), a pathological marker of cardiomyocyte cell death³¹⁻³³ (**Fig. S9d**). Together, these
403 observations provide initial pathological evidence that SARS-CoV-2 infects the human heart and
404 may contribute to cardiomyocyte cell death and myocardial inflammation that is distinct from
405 lymphocytic myocarditis.
406

407 **Discussion:**

408 Cardiac manifestations of COVID-19 including myocardial injury (elevated troponin),
409 reduced left ventricular systolic function, and arrhythmias are increasingly recognized as
410 important determinants of morbidity and mortality^{3,8}. Moreover, imaging studies have uncovered
411 evidence of chronic myocardial pathology among both hospitalized and ambulatory patients,
412 suggesting the potential for long-term consequences of COVID-19^{5,6}. Little is understood
413 regarding the etiology of these conditions. To gain insight into the cardiac complications of
414 COVID-19, we developed a human EHT system that recapitulates many features of SARS-CoV-
415 2 induced myocarditis. We provide evidence that SARS-CoV-2 infects hPSC-derived CMs,
416 resulting in reduced metabolic and contractile apparatus gene expression, sarcomeric
417 disassembly, inflammatory signaling, and cell death. Viral entry was ACE2-dependent and relied
418 on endosomal cysteine protease activity. Our findings are consistent with a recent report
419 suggesting that SARS-CoV-2 infects human cardiac slices and hPSC-derived CMs in an ACE2
420 and cathepsin dependent manner³⁴. We extend these observations to show that cardiomyocytes
421 supported viral replication, rapidly produced infectious virions, activated type I IFN signaling, and
422 displayed cytopathic features seen with coronavirus infection. Infected EHTs demonstrated
423 reduced contractile force, sarcomere disassembly, and pathological evidence of myocarditis
424 including macrophage activation. Examination of human autopsy and endomyocardial biopsy
425 tissue from individuals diagnosed with COVID-19 myocarditis revealed similar findings of
426 cardiomyocyte infection, cell death, and macrophage infiltration.

427 Whether cardiac manifestations of COVID-19 are a result of viral infection or exuberant
428 systemic inflammation remains a debated topic. It is also possible that microvascular thrombosis
429 may contribute to cardiac events. We provide evidence that SARS-CoV-2 readily infects and
430 replicates within human cardiomyocytes, indicating that viral infection likely contributes to the
431 pathogenesis of COVID-19 myocarditis. SARS-CoV-2 was unable to replicate in other cell types
432 found within the left ventricular myocardium including cardiac fibroblasts, endothelial cells, and

433 macrophages. It remains possible that SARS-CoV-2 could also infect other cardiac cell types that
434 are difficult to isolate from the human heart or produce through directed differentiation protocols,
435 such as pericytes and endocardial cells. Despite these limitations, our findings clearly
436 demonstrate that cardiomyocytes are a target of SARS-CoV-2 infection.

437 Consistent with this conclusion, examination of human autopsy and endomyocardial
438 biopsy tissue obtained from four patients with clinical diagnoses of COVID-19 myocarditis
439 revealed evidence of myocardial SARS-CoV-2 RNA and protein predominately within
440 cardiomyocytes and accumulation of macrophages in areas surrounding myocardial injury. These
441 findings are consistent with prior reports highlighting infiltration of monocytes, lymphocytes, and
442 plasma cells in an endomyocardial biopsy specimen from a patient with suspected COVID-19
443 myocarditis³⁵ and viral RNA within the myocardium of COVID-19 autopsy specimens³⁶. It is
444 important to note that the human specimens examined in this study differ substantially from
445 published autopsy series that did not include subjects with cardiac manifestations^{3,37}. Here, we
446 exclusively focused on subjects with active COVID-19 infection and clinical evidence of
447 myocarditis based on echocardiography and clinical presentation.

448 Numerous studies have reported that extrapulmonary cell types are susceptible to SARS-
449 CoV-2 infection³⁸⁻⁴⁰. This broader cellular tropism appears to be dictated by ACE2 expression
450 and the ability of the virus to gain access to extrapulmonary tissues. Among cell types within the
451 heart, cardiomyocytes and pericytes express ACE2 mRNA¹⁷. Our immunostaining studies of
452 human heart samples and EHTs suggest that ACE2 protein is most prominently expressed in
453 cardiomyocytes. Using a human ACE2 neutralizing antibody, we demonstrated that ACE2 is
454 essential for SARS-CoV-2 to infect cardiomyocytes. It is not yet clear at what stage during the
455 course of their differentiation developing cardiomyocytes become permissive to SARS-CoV-2
456 infection. Furthermore, it remains to be explored whether cardiomyocyte maturation, remodeling,
457 and/or subset diversification might impact vulnerability or host responses to viral infection. This
458 possibility is supported by the heterogeneous expression of ACE2 in the human heart and hPSC-

459 derived CMs, and may explain why pre-existing cardiovascular disease represents such a strong
460 risk factor for COVID19 mortality. Consistent with this idea, ACE2 expression is increased in heart
461 failure^{28,41}. hPSC-derived CMs and EHTs offer an opportunity to address these important
462 questions. Indeed, a previous study demonstrated that hPSC-derived cells (including
463 cardiomyocytes) can support SARS-CoV-2 infection⁴⁰. Whether SARS-CoV-2 enters the heart
464 through hematological seeding and/or direct extension from the pleural cavity remains unknown.

465 Emerging data suggests that SARS-CoV-2 can enter cells either directly through the
466 plasma membrane using TMPRSS2 or through endosomal pathways via cathepsins, and that the
467 utilization of these pathways is cell-type dependent^{15,16}. We demonstrate that SARS-CoV-2
468 depends almost exclusively upon the endosomal pathway for entry into hPSC-derived CMs, which
469 is consistent with the greater abundance of transcripts for endosomal cathepsins relative to
470 TMPRSS2 and TMPRSS4 transcripts. As such, hPSC-derived CMs may be informative for the
471 development and testing of drugs that target viral cell entry. Based on this, we predict that
472 compounds targeting endosomal viral entry would have greater efficacy in preventing COVID-19
473 cardiac infection than those targeting TMPRSS2 or related proteases.

474 EHTs provided an opportunity to gain mechanistic insights into the relationship between
475 cardiomyocyte infection, myocardial inflammation, and contractile dysfunction. Infection of EHTs
476 resulted in generation of inflammatory mediators, reduced ACE2 expression, cardiomyocyte cell
477 death, disrupted sarcomeric structure, and changes in sarcomeric and metabolic gene
478 expression. Each of these mechanisms likely contribute to reduced EHT contractility. We
479 demonstrated that cardiomyocyte infection is essential for inflammatory gene expression,
480 sarcomere loss, and cell death. Intriguingly, blockade of viral nucleic acid sensing pathways
481 (TBK1 inhibitor) blunted reductions in sarcomere gene expression. However, sarcomere
482 disassembly in infected cells and cardiomyocyte cell death was not impacted. These findings
483 highlight the central role of cardiomyocyte infection and suggest that targeting pathways that are
484 responsible for sarcomere breakdown may improve outcomes in patients with cardiac

485 complications of COVID-19. However, our findings do not exclude an important role for
486 inflammation in COVID-19 myocarditis. The relevance of ACE2 downregulation in infected
487 cardiomyocytes will require further clarification as *Ace2*^{-/-} mice display left ventricular systolic
488 dysfunction and heart failure⁴².

489 Effectively targeting the inflammatory response to SARS-CoV-2 infection in the heart will
490 require a careful dissection of the cell types involved and identification of key effector pathways.
491 Macrophages and fibroblasts appear to contribute to the inflammatory response. Despite low
492 levels of ACE2 expression and resistance to SARS-CoV-2 infection, macrophages and fibroblasts
493 each generated inflammatory chemokines and cytokines in response to exposure to SARS-CoV-
494 2 in 2D culture, a response likely driven by recognition of viral RNAs and/or proteins. The addition
495 of fibroblasts and macrophages to 2D engineered heart tissues exaggerated production of
496 immune-related mRNAs following exposure to SARS-CoV-2. While this response could be a
497 result of direct recognition of viral RNAs and proteins by fibroblasts and macrophages, additional
498 mechanisms of macrophage and fibroblast activation should be considered such as
499 communication between infected cardiomyocytes and adjacent macrophages and fibroblasts
500 through either the production of soluble mediators or intercellular transfer via gap junctions. Future
501 studies are necessary to dissect the cellular mechanisms and signaling pathways that initiate and
502 potentiate local inflammation between infected cardiomyocytes and surrounding macrophages,
503 fibroblasts, and other cell types.

504 EHTs have been considered as models for dilated and hypertrophic cardiomyopathies
505 given their genetic etiologies^{43,44}. Here, we developed a human EHT model of viral myocarditis.
506 EHTs infected with SARS-CoV-2 recapitulated several features of viral myocarditis including
507 cardiomyocyte infection, cell death, inflammation, and contractile dysfunction. These EHTs
508 contained hPSC-derived CMs, monocyte-derived macrophages, and fibroblasts to mirror some of
509 the cellular and extracellular constituents of the human myocardium. To our knowledge,
510 macrophages have not been previously incorporated into human EHTs. Given recent advances

511 in stem cell differentiation protocols, incorporation of tissue resident macrophages, endothelial
512 cells, and cardiac fibroblasts is on the horizon and could further strengthen this model system^{45,46}.
513 Moreover, it is possible to genetically modify each of these cellular components to gain
514 mechanistic insights into the pathogenesis of various diseases including COVID-19 myocarditis.
515 These observations add to an emerging field that have successfully utilized EHT systems for
516 testing of compounds for cardiotoxicity and efficacy^{47,48}. From a broader perspective, our findings
517 are consistent with the emerging utility of human organoid systems in the investigation of SARS-
518 CoV-2^{38,39,49,50}.

519 Our study is not without limitations, including limited autopsy and biopsy tissue availability,
520 inherent immaturity of hPSC-derived CMs, and incomplete representation of human myocardial
521 cell types included in EHTs. Nonetheless, our experiments support the conclusion that SARS-
522 CoV-2 infection of cardiomyocytes and resultant myocardial injury and inflammation likely
523 promote or contribute to cardiac manifestations. We provide evidence that human EHTs
524 recapitulate many features of COVID-19 myocarditis, demonstrate that SARS-CoV-2 infection of
525 EHTs can produce multiscale changes spanning from the molecular to functional levels, and show
526 that EHTs serve as useful tools for dissecting mechanisms that contribute to cardiac pathology.
527

528 **Methods:**

529

530 ***Biosafety.*** All aspects of this study were approved by the office of Environmental Health and
531 Safety at Washington University School of Medicine prior to the initiation of this study. Work with
532 SARS-CoV-2 was performed in a BSL-3 laboratory by personnel equipped with powered air
533 purifying respirators (PAPR).

534

535 ***Viruses.*** The 2019n-CoV/USA_WA1/2019 isolate of SARS-CoV-2 was obtained from the United
536 States Centers for Disease Control (CDC). The mNeonGreen SARS-CoV-2 virus was published
537 recently¹⁸. Infectious stocks were grown by inoculating Vero CCL81 cells and collecting
538 supernatant upon observation of cytopathic effect. Debris was removed by centrifugation and
539 passage through a 0.22 µm filter. Supernatant was then aliquoted and stored at -80°C. All
540 infections were performed at a multiplicity of infection (MOI) of 0.1. The mNeonGreen SARS-CoV-
541 2 virus stock used in this study was subjected to deep sequencing using ARTIC⁵¹ and found to
542 have a mutation in the furin cleavage site (positions 23606-23608 of NC_045512.2) at a combined
543 frequency of 31%.

544

545 ***Focus forming assay.*** Vero E6 cells were seeded at a density of 4×10^4 cells per well in flat-
546 bottom 96-well tissue culture plates. The following day, media was removed and replaced with
547 100 µL of 10-fold serial dilutions of the material to be titered. Two hours later, 135 µL of
548 methylcellulose overlay was added. Plates were incubated for 48 h, then fixed with 4%
549 paraformaldehyde (final concentration) in phosphate-buffered saline for 20 min, followed by
550 permeabilization with saponin-containing buffer. Plates were incubated overnight at 4°C in 100
551 µL of permeabilization buffer containing 1 µg/mL of the CR3022 anti-spike monoclonal antibody⁵².
552 Following washing, 50 µL of goat anti-human secondary antibody conjugated to HRP (Sigma
553 AP504P), diluted 1:1000 in permeabilization buffer, was added for 2 hours at room temperature

554 with shaking. Foci were stained with 50 μ L of KPL Trueblue (SeraCare), then scanned and
555 automatically quantitated on a Biospot plate reader (Cellular Technology Limited).

556

557 **Quantitative RT-PCR.** RNA was extracted using the MagMax mirVana Total RNA isolation kit
558 (Thermo Scientific) on the Kingfisher Flex extraction robot (Thermo Scientific). RNA was reverse
559 transcribed and amplified using the TaqMan RNA-to-CT 1-Step Kit (ThermoFisher). Reverse
560 transcription was carried out at 48°C for 15 min followed by 2 min at 95°C. Amplification was
561 accomplished over 50 cycles as follows: 95°C for 15 s and 60°C for 1 min. Copies of SARS-CoV-
562 2 N gene RNA in samples were determined using a previously published assay⁵³. Briefly, a
563 TaqMan assay was designed to target a highly conserved region of the N gene (Forward primer:
564 ATGCTGCAATCGTGCTACAA; Reverse primer: GACTGCCGCCTCTGCTC; Probe: /56-
565 FAM/TCAAGGAAC/ZEN/AACATTGCCAA/3IABkFQ/). This region was included in an RNA
566 standard to allow for copy number determination down to 10 copies per reaction. The reaction
567 mixture contained final concentrations of primers and probe of 500 and 100 nM, respectively. For
568 host genes (ACE2, TMPRSS2, OAS1, MX1, TNF), RNA was reverse-transcribed using the High
569 Capacity cDNA Reverse Transcription Kit (ThermoFisher) and amplified using SYBR Green
570 system (ThermoFisher) with beta2 microglobulin as an internal reference gene.

571

572 **Quantification of ACE2 expression in RNA-Seq.** We performed a differential gene expression
573 analysis using R package DESeq2⁵⁴ on the Care4DCM cohort⁵⁵. The DESeq2 package utilizes
574 negative binominal distribution to model the distribution of RNA-Seq reads, and uses Wald test to
575 calculate p-values⁵⁴. The Care4DCM cohort included 60 DCM patients and 35 controls⁵⁵. Of the
576 60 DCM patients, 52 received ACEI and 8 received ARB. The myocardial biopsies were extracted
577 from the LV apex by heart catheterization and preserved in liquid nitrogen following standardized
578 protocols. The RNA was extracted from the cardiac tissues using Allprep Kits (Qiagen,

579 Düsseldorf, Germany), then the RNA sequencing was carried out using the TrueSeq RNA Sample
580 Prep Kit (Illumina, San Diego, California, USA)⁵⁵.

581

582 **Human atrial tissue samples.** The study protocol involving human tissue samples was approved
583 by the ethics committees of the Medical Faculty of Heidelberg University (Germany; S-017/2013).
584 Written informed consent was obtained from all patients and the study was conducted in
585 accordance with the Declaration of Helsinki. Tissue samples of right atrial appendages (RAA)
586 were obtained from patients undergoing open heart surgery for coronary artery bypass grafting
587 or valve repair /replacement in the local heart surgery department.

588

589 **Atrial and ventricular cardiomyocyte isolation.** After excision, tissue samples were
590 immediately placed into preoxygenated transport solution (100 mM NaCl, 10 mM KCl, 1.2 mM
591 KH₂PO₄, 5 mM MgSO₄, 50 mM taurine, 5 mM 3-[N-morpholino] propane sulfonic acid [MOPS],
592 30 mM 2,3-butanedione monoxime and 20 mM glucose, pH 7.0 with NaOH) and subjected to
593 cardiomyocyte isolation within 15 minutes. RAA tissue samples were dissected into small pieces
594 and rinsed 3 times in Ca²⁺-free Tyrode's solution (100 mM NaCl, 10 mM KCl, 1.2 mM KH₂PO₄,
595 5 mM MgSO₄, 50 mM taurine, 5 mM 3-(N-morpholino) propane sulfonic acid (MOPS), and 20 mM
596 glucose, pH 7.0 with NaOH) supplemented with 2,3-butanedione monoxime (30 mM BDM; Sigma-
597 Aldrich, St. Louis, MO, USA). The solutions were oxygenated with 100 % O₂ at 37°C. After
598 digestion with collagenase type I (288 U/ml; Worthington) and protease type XXIV (5 mg/ml;
599 Sigma-Aldrich) for 15 min and agitation in protease-free solution for another 35 min, the cell
600 suspension was filtered through a 200 nm mesh. Subsequently the Ca²⁺ concentration of the cell
601 fraction was increased to 0.2 mM, the cell suspension was centrifuged and calcium tolerant rod-
602 shaped single cardiomyocytes were declared as the cardiomyocyte fraction (CM). Remaining
603 tissue chunks were declared as the non cardiomyocyte (NM) fraction. Cells were stored in TRIzol-
604 Reagent (ThermoFisher) at -20°C. Isolation of total RNA was performed, using TRIzol-Reagent

605 (ThermoFisher) and frozen tissue samples were processed according to the manufacturer's
606 protocol. Synthesis of single-stranded cDNA was carried out with the Maxima First Strand cDNA
607 Synthesis Kit (ThermoFisher), using 3 µg of total RNA per 20 µl reaction. For quantitative real-
608 time PCR (qPCR) 10 µl reactions, consisting of 0.5 µl cDNA, 5 µl TaqMan Fast Universal Master
609 Mix (ThermoFisher), and 0.5 µl 6-carboxyfluorescein (FAM)-labeled TaqMan probes and primers
610 (TaqMan Gene Expression Assays; ThermoFisher) were analyzed using the StepOnePlus
611 (Applied Biosystems, Foster City, CA, USA) PCR system. hACE2 primers and probes
612 (Hs01085333_m1) were purchased from ThermoFisher. The glyceraldehyde 3-phosphate
613 dehydrogenase housekeeping gene (GAPDH: Hs99999905_m1) was used for normalization. All
614 RT-qPCR reactions were performed as triplicates and control experiments in the absence of
615 cDNA were included. Means of triplicates were used for the $2^{-\Delta Ct}$ calculation, where $2^{-\Delta Ct}$
616 corresponds to the ratio of mRNA expression versus GAPDH.

617

618 **Flow cytometry.** Cells were dissociated to single-cell suspension with 0.25% trypsin (Gibco),
619 then washed and incubated with Zombie-violet viability stain (Biolegend) at a dilution of 1:500 in
620 100 µL of PBS at room temperature. In some assays, antibodies against surface proteins were
621 incubated with the cells. Fibroblasts were identified using anti-CD90 PE (Biolegend, catalog
622 number 328110) and macrophages were identified using anti-CD14 APC (Biolegend, catalog
623 number 367118). Cells then were fixed with 4% paraformaldehyde (final concentration) in
624 phosphate-buffered saline for 20 min and analyzed on the MACSQuant 10 (Miltenyi Biotec) or the
625 LSRFortessa X20 (Becton Dickinson Biosciences). Analysis was performed using FlowJo 10.6.1
626 (Becton Dickinson & Co).

627

628 **hPSC culture and cardiomyocyte differentiation.** The parent stem cell line, BJFF.6, was
629 generated from the human BJ fibroblast line (ATCC, catalog number: CRL-2522) by the Genome
630 Engineering and iPSC Center at Washington University in St. Louis. This parent cell line has no

631 known mutations associated with heart disease and the stem cells are pluripotent as assessed
632 by immunofluorescence staining⁵⁶. Differentiation to hPSC-derived CMs was performed as
633 previously described ⁵⁶. Briefly, stem cells were maintained in feeder-free culture and
634 differentiation was initiated by temporal manipulation of WNT signaling^{57,58}. hPSC-derived CMs
635 were enriched using metabolic selection ⁵⁹, yielding >90% cardiomyocytes ⁵⁶. All experiments
636 were conducted at least 30 days after the initiation of differentiation.

637

638 ***Differentiation (and validation) of stem cell derived cardiac fibroblasts.*** hPSC derived
639 cardiac fibroblasts were differentiated using the method of Zhang et al. (reference ⁴⁵). Briefly,
640 differentiation was initiated by directing the BJFF stem cell line towards a mesoderm/cardiac
641 progenitor lineage by the activation and subsequent inhibition of WNT signaling using CHIR-
642 99021 and IWP2 respectively. These cells were then directed to become proepicardial cells by
643 the addition of retinoic acid and WNT CHIR 99021 followed by TGF β inhibition (SB431542, Tocris
644 Bioscience 1614). Finally, the pro-epicardial cells were directed to become quiescent cardiac
645 fibroblasts by the addition of FGF2 and higher levels of TGF β inhibition. Derivation of hPSC-
646 cardiac fibroblasts was validated by measuring gene expression using RT-PCR. They showed
647 high levels of both cardiac specific genes, GATA4 and TCF21 as well as general fibroblast genes
648 COL1A1 and DDR2 (Fig. S1c).

649

650 ***Fibroblast culture.*** BJ fibroblasts (ATCC, catalog number: CRL-2522) were cultured in Eagle's
651 Minimum Essential Medium with 10% FBS and 1% Pen-Strep (Gibco, catalog number:
652 15140122). Human ventricular cardiac fibroblasts that were harvested from normal adult
653 ventricular tissue were obtained from Lonza, maintained at low passage number (<12), and
654 cultured according to the manufacturer's recommendations in FGM-3 growth media.

655

656 **Macrophage culture.** CD34⁺ cells isolated from human cord blood were cultured in Iscove's
657 Modified Dulbecco's Medium with 10% FBS, 1% Pen-Strep, and 10 ng/mL of human macrophage
658 colony stimulating factor (M-CSF, R&D Systems, catalog number 216-MC) for at least 10 days to
659 generate mature macrophages before use in experiments.

660

661 **Endothelial cell culture.** H1 hPSCs were differentiated into vascular endothelial cells following
662 the published protocol⁶⁰. Arterial endothelium was identified as CD34+CD184+CD73+ cells using
663 appropriate antibodies (BD Biosciences, anti-CD34 PE-Cy7 [cat # 560710], anti-CD184 APC [cat
664 #560936], anti-CD73 PE [cat #550257]) and isolated by flow cytometric cell sorting on a BD
665 FACS AriaII. These cells were cultured in StemPro-34 serum free media (ThermoFisher, cat#
666 10639011).

667

668 **Isolation of primary human cardiac endothelial cells and macrophages.** Human myocardium
669 was dissected into ~200mg pieces and digested in 3mL DMEM containing 250U/mL collagenase
670 IV, 60U/mL hyaluronidase and 60U/mL DNaseI for 45 minutes at 37 degrees C. Following digest
671 and red blood cell lysis, the resultant single cell suspension was incubated with anti-CD14 PE
672 (cat #301806), anti-CD64 PE-Cy7 (cat #305022), anti-CD45 FITC (cat #304006), and anti-CD31
673 BV421 (cat #303124) (all antibodies from Biolegend). Macrophages were identified as
674 CD14+CD64+CD45+ cells and endothelial cells were identified as CD31+CD64-CD45- cells.
675 Cells were isolated by flow cytometric cell sorting on a BD FACSMelody and cultured in StemPro-
676 34 supplemented with either M-CSF or VEGF (R&D Systems, cat #293-VE).

677

678 **Two-dimensional cell cultures and tissues.** hPSC-derived CMs, fibroblasts, and/or
679 macrophages were dissociated from two-dimensional cultures using 0.25% Trypsin-EDTA,
680 resuspended in media containing RPMI-1640 with 20% FBS and 10 μM Y-27632 and plated on
681 gelatin coated tissue culture dishes. After 48 h, the media was changed to DMEM High glucose

682 (4 mg/mL), 10% FBS, 1% non-essential amino acids, 1% GlutaMAX Supplement, and 1% Pen-
683 Strep. All drug compounds were purchased from Selleckchem (ruxolitinib, catalog number S8932;
684 MRT67307, catalog number S7948; E64, catalog number S7379; camostat, catalog number
685 S2874) and resuspended to a stock concentration of 10 μ M in PBS or DMSO (depending on the
686 solubility profile), then diluted to working concentration in culture media (described above) and
687 sterile-filtered.

688

689 ***Immunostaining of hPSC-derived CMs and confocal fluorescence microscopy.***

690 Immunostaining was performed as previously described with a few modifications⁵⁶. Briefly,
691 cardiomyocytes were fixed for 20 minutes in 4% formaldehyde in phosphate buffered saline
692 (PBS). Cells were then permeabilized with 0.4% Triton X-100 for 20 minutes at room temperature.
693 The cells were blocked for 1 hour using a blocking solution containing 3% bovine serum albumin,
694 5% donkey serum, 0.1% Triton X-100, and 0.02% sodium azide in PBS. Primary antibodies (rabbit
695 anti Troponin T, 1:400, Abcam, ab45932) were added for 1-2 hours at room temperature or
696 overnight at 4 °C. Cells were then washed with PBS before incubating for 1 hour in secondary
697 antibody (Cy3 donkey anti-rabbit, Jackson Immunoresearch, 711165152). 4',6-diamidino-2-
698 phenylindole (DAPI) was used at a 1:50000 dilution to stain for nuclei. Cells were visualized using
699 a Nikon A1Rsi confocal microscope (Washington University Center for Cellular Imaging). Z-
700 stacks of cells with 40x magnification were recorded in sequential scanning mode. Images were
701 processed in ImageJ and Z-stacks were converted to standard deviation projections⁶¹.

702

703 ***Engineered heart tissues (EHTs).*** EHTs were prepared according to published protocol⁶² with
704 modifications. Casting molds for tissue formation were prepared using PDMS at a 1:25 ratio. 1
705 mL of PDMS was poured into each well of a 24-well plate and a Teflon spacer (EHT Technologies
706 GmbH; Hamburg, Germany) was placed inside to generate a well. The PDMS was degassed

707 under high vacuum and baked overnight at 65°C. The Teflon spacers were removed using
708 ethanol.

709 Prior to use, the casting molds were sterilized with ethanol, dried with nitrogen gas, and placed
710 under UV light for 10-15 min. 1% pluronic-F127 in PBS was added to the molds for 20 min to
711 block the surface from adhering to the seeded tissues. The pluronic was removed, the casting
712 molds were rinsed twice with PBS, and then dried. Silicone racks consisting of two pairs of PDMS
713 posts (EHT Technologies GmbH, Hamburg, Germany) were positioned such that each pair of
714 PDMS posts fit within one casting mold.

715 The procedure for seeding of tissues was modified from⁶². Working on ice, rat collagen I (1 mg/mL
716 final concentration) was combined with equal parts 2x DMEM containing FBS and neutralized
717 with sodium hydroxide. Growth factor reduced Matrigel (Corning, catalog number: 354230) was
718 added to a final concentration of 0.77 g/mL. hPSC-derived CMs, fibroblasts, and/or macrophages
719 were dissociated from two-dimensional cultures with 0.25% Trypsin-EDTA and the Trypsin was
720 quenched in RPMI-1640 with 20% FBS media containing 10 g/mL of DNaseI. Cells were then
721 centrifuged, resuspended in media containing RPMI-1640 with 20% FBS and 10 μ M Y-27632,
722 and combined with the collagen/Matrigel mixture. Each tissue contained 10⁶ hPSC-derived CMs,
723 5% fibroblasts, and 10% macrophages. Tissues were seeded in the casting molds with the
724 silicone racks in a 100 μ L volume. After polymerizing around the silicone racks for 2 h at 37°C,
725 the tissues were covered overnight with RPMI-1640 containing 20% FBS. The tissues, attached
726 to the posts of the silicone racks, then were moved out of the casting molds and transferred into
727 media containing DMEM High glucose (4 mg/mL), 10% FBS, 1% non-essential amino acids, 1%
728 GlutaMAX Supplement, and 1% Pen-Strep. Consistent with previous reports, engineered heart
729 tissue contraction was observed ~2-5 days after seeding, and the displacement increased over
730 time as the tissues organize and mature⁶². By day 7 post seeding, all tissues generated at
731 least 0.025 mm of displacement (see details below). EHTs were inoculated with SARS-CoV-2 at

732 least 7 days after tissue seeding, and EHT contraction and morphology were measured daily
733 throughout the course of the experiment.

734

735 ***Analysis of engineered heart tissue contractility.*** EHTs between two PDMS posts were
736 visualized on an EVOS microscope and videos of spontaneously contracting posts were recorded
737 at 30 frames per second using a Macintosh desktop with built-in camera (**Supplementary Videos**
738 **1 and 2**). We used the 2 mm diameter of the caps on the posts to calibrate the pixels per mm for
739 each video. We wrote a custom script in MATLAB to calculate the displacement of the posts as a
740 function of time. Automated tracking was done using the computer vision toolbox and the
741 displacement was calculated as a function of time. A second order polynomial spline fit was
742 applied to remove any drift in the camera position. Traces were smoothed using a Savitsky-Golay
743 filter and peaks in the displacement were identified using the findpeaks algorithm. The average
744 and standard deviation of the displacement was then calculated for each ~60 sec video. The time
745 for force development was defined as the time required to achieve 75% activation and the time
746 for relaxation was defined as the time to relax to 75% of the peak activation.

747

748 ***Histology of autopsy and engineered heart tissues.*** Tissues were fixed with 10% NBF for 7
749 days, embedded in 1% agar, mounted in cassettes, and embedded in paraffin. Target markers
750 were visualized using Opal 4-Color Manual IHC Kit (Perkin-Elmer) with the following changes: 1)
751 10% NBF fixation step was substituted for treatment with 10% MeOH + 10% hydrogen peroxide
752 in water for 20 min; 2) during antigen retrieval, the vessel with AR6 was brought to boiling and
753 slides were immediately transferred into deionized water; 3) blocking buffer was substituted for
754 10% FBS in TBST. Primary antibodies against human sarcomeric actin (Sigma A2127), human
755 Troponin T (ThermoFisher MS-295-P1), human CD68 (BioRad MCA5709), human ACE2 (Abcam
756 ab15348), human Ki67 (Abcam ab16667), human CCR2 (Abcam ab176390), SARS-CoV-2-N

757 (Sino Biological 40143-R001) were used. Cell death was assessed using TUNEL staining from *In*
758 *Situ* Cell Death Detection Kit (Roche) with Opal-based costain for sarcomeric actin as described
759 above. Viral RNA was directly visualized with RNAscope Multiplex Fluorescent Reagent Kit v2
760 Assay (Advanced Cell Diagnostics) and RNAscope 2.5 HD Detection Reagent - RED (Advanced
761 Cell Diagnostics) using positive-strand and negative strand probes for ORF1ab. Images were
762 collected on a confocal microscope (Zeiss LSM 700 Laser Scanning Confocal) and processed
763 using ZenBlack (Zeiss) and ImageJ (NCBI). Troponin staining was quantified using manual cell
764 tracing in ImageJ (NCBI) from at least three areas and 30 cells analyzed per tissue.

765

766 ***Electron microscopy.*** Cells grown on aclar coverslips were briefly rinsed in 0.15 M cacodylate
767 buffer that was warmed to 37°C followed by the addition of 2.5% glutaraldehyde, 2%
768 paraformaldehyde, 0.2% tannic acid in 0.15 M cacodylate buffer with 2 mM CaCl₂, pH 7.4 at 37°C.
769 Once added, the coverslips were returned to a 37°C incubator for 15 min followed by overnight
770 fixation at room temperature. Post fixation, samples were rinsed in 0.15 M cacodylate buffer 4
771 times for 15 min each followed by a secondary fixation in 1% OsO₄/1.5% K₃Fe(CN)₆ in 0.15 M
772 cacodylate buffer for 1.5 h in the dark. The coverslips were then rinsed 4 times in ultrapure water
773 for 15 min each followed by *en bloc* staining with 2% aqueous uranyl acetate overnight at 4°C in
774 the dark. After another 4 water washes, the samples were dehydrated in a graded ethanol series
775 (30%, 50%, 70%, 90%, 100% x4) for 10 min for each step. Once dehydrated, cells were infiltrated
776 with LX112 resin over a period of 2 days. The coverslips then were flat embedded and
777 polymerized at 60°C for 48 h. Once polymerized, the aclar coverslips were peeled away from the
778 resin, and small areas were excised and mounted perpendicularly on a blank epoxy stub for cross
779 sectioning. 70 nm sections were then cut and imaged on a TEM (JEOL JEM-1400 Plus) at 120
780 KeV.

781

782 **RNA sequencing and analysis.** Samples were prepared according to library kit manufacturer's
783 protocol, indexed, pooled, and sequenced on an Illumina NovaSeq 6000. Basecalls and
784 demultiplexing were performed with Illumina's bcl2fastq software and a custom python
785 demultiplexing program with a maximum of one mismatch in the indexing read. RNA-seq reads
786 were then aligned to the Human Ensembl GRCh38.76 primary assembly and SARS-CoV-2 NCBI
787 NC_045512 Wuhan-Hu-1 genome with STAR version 2.5.1a⁶³. Gene counts were derived from
788 the number of uniquely aligned unambiguous reads by Subread:featureCount version 1.4.6-p5⁶⁴.
789 Isoform expression of known Ensembl transcripts were estimated with Salmon version 0.8.2⁶⁵.
790 Sequencing performance was assessed for the total number of aligned reads, total number of
791 uniquely aligned reads, and features detected. The ribosomal fraction, known junction saturation,
792 and read distribution over known gene models were quantified with RSeQC version 2.6.2⁶⁶.

793 All gene counts were imported into the R/Bioconductor package EdgeR⁶⁷ and TMM normalization
794 size factors were calculated to adjust for samples for differences in library size. Ribosomal genes
795 and genes not expressed in at least four samples greater than one count-per-million were
796 excluded from further analysis. The TMM size factors and the matrix of counts were then imported
797 into the R/Bioconductor package Limma⁶⁸. Weighted likelihoods based on the observed mean-
798 variance relationship of every gene and sample were then calculated for all samples with the
799 voomWithQualityWeights⁶⁹. The performance of all genes was assessed with plots of the residual
800 standard deviation of every gene to their average log-count with a robustly fitted trend line of the
801 residuals. Differential expression analysis was then performed to analyze for differences between
802 conditions and the results were filtered for only those genes with Benjamini-Hochberg false-
803 discovery rate adjusted p-values less than or equal to 0.05.

804 For each contrast extracted with Limma, global perturbations in known Gene Ontology (GO)
805 terms, MSigDb, and KEGG pathways were detected using the R/Bioconductor package GAGE⁷⁰
806 to test for changes in expression of the reported log 2 fold-changes reported by Limma in each

807 term versus the background log 2 fold-changes of all genes found outside the respective term.
808 The R/Bioconductor package heatmap3⁷¹ was used to display heatmaps across groups of
809 samples for each GO or MSigDb term with a Benjamini-Hochberg false-discovery rate adjusted
810 p-value less than or equal to 0.05. Perturbed KEGG pathways where the observed log 2 fold-
811 changes of genes within the term were significantly perturbed in a single-direction versus
812 background or in any direction compared to other genes within a given term with p-values less
813 than or equal to 0.05 were rendered as nnotated KEGG graphs with the R/Bioconductor package
814 Pathview⁷².

815 To find the most critical genes, the raw counts were variance stabilized with the R/Bioconductor
816 package DESeq2⁵⁴ and then analyzed via weighted gene correlation network analysis with the
817 R/Bioconductor package WGCNA⁷³. Briefly, all genes were correlated across each other by
818 Pearson correlations and clustered by expression similarity into unsigned modules using a power
819 threshold empirically determined from the data. An eigengene was created for each de novo
820 cluster and its expression profile was then correlated across all coefficients of the model matrix.
821 Because these clusters of genes were created by expression profile rather than known functional
822 similarity, the clustered modules were given the names of random colors where grey is the only
823 module that has any pre-existing definition of containing genes that do not cluster well with others.
824 These *de novo* clustered genes were then tested for functional enrichment of known GO terms
825 with hypergeometric tests available in the R/Bioconductor package clusterProfiler⁷⁴. Significant
826 terms with Benjamini-Hochberg adjusted p-values less than 0.05 were then collapsed by similarity
827 into clusterProfiler category network plots to display the most significant terms for each module
828 of hub genes in order to interpolate the function of each significant module. The information for
829 all clustered genes for each module were combined with their respective statistical significance
830 results from Limma to identify differentially expressed genes.

831

832 **Statistical analysis.** Statistical tests were chosen based on standards in the virology and
833 cardiomyocyte fields for given assay. Parametric and non-parametric statistical methods were
834 used when appropriate. Statistical significance was assigned when P values were < 0.05 using
835 Prism Version 8 (GraphPad). Specific tests are indicated in the figure legends.

836 **Data availability.** All data supporting the findings of this study are found within the paper and its
837 Extended Data Figures and are available from the corresponding authors upon request. RNA
838 sequencing data sets generated in this study will be made available in GEO at the time of
839 publication.

840 **Acknowledgements:**

841 The authors would like to acknowledge funding support from the National Institutes of Health
842 (R01HL141086 to M.J.G, R01 HL138466 to K.J.L., R01 HL139714 to K.J.L., 75N93019C00062
843 and R01 AI127828 to M.S.D.), Burroughs Welcome Fund (1014782 to K.J.L.), Defense Advanced
844 Research Project Agency (HR001117S0019), the March of Dimes Foundation (FY18-BOC-
845 430198 to M.J.G.), Foundation of Barnes-Jewish Hospital (8038–88 to K.J.L.), and Children’s
846 Discovery Institute of Washington University and St. Louis Children’s Hospital (CH-II-2017–628
847 to K.J.L., PM-LI-2019-829 to K.J.L. and M.J.G.). Imaging was performed in the Washington
848 University Center for Cellular Imaging (WUCCI) which is funded, in part by the Children’s
849 Discovery Institute of Washington University and St. Louis Children’s Hospital (CDI-CORE-2015-
850 505 and CDI-CORE-2019-813) and the Foundation for Barnes-Jewish Hospital (3770). The
851 authors thank Dr. Cynthia Goldsmith for help interpreting electron microscopy micrographs and
852 the McDonnell Genome Institute (MGI) at Washington University School of Medicine for
853 assistance in performing sequencing and analysis.

854

855 **Conflicts of interest/Competing interests:**

856 Kory Lavine - Medtronic: DT-PAS/APOGEE trial advisory board. M.S.D. is a consultant for Inbios,
857 Eli Lilly, Vir Biotechnology, NGM Biopharmaceuticals, and on the Scientific Advisory Board of
858 Moderna. The Lavine laboratory has received funding and unrelated sponsored research
859 agreements from Amgen. The Diamond laboratory has received funding and unrelated sponsored
860 research agreements from Moderna, Vir Biotechnology, and Emergent BioSolutions. Lina
861 Greenberg, W. Tom Stump, Michael Greenberg, Adam Bailey, Oleksandr Dmytrenko, Andrea
862 Bredemeyer - None.

863

864

865 **Author Contributions:**

866 Conceptualization, M.J.G, A.L.Bailey, K.L, M.S.D.; Methodology, L.G., W.T.S., A.L.Bailey;

867 Software, M.J.G.; Investigation, L.G., O.D., A.L.Bailey, A.L.Bredemeyer, P.M., J.L., V.P., E.W.,

868 S.S, J.A.F., W.G., C.S.; Resources, E.B., A.J.N, K.A.H., A.S.R, M.S., D.H., X.X., P-Y.S, J.T.H,

869 F.L., W.T.S., L.S.; Writing – Original Draft, L.G., M.J.G., A.L.Bailey, K.L., O.D., A.L.Bredemeyer;

870 Writing – Review & Editing, L.G., M.J.G., A.L.Bailey, K.L., O.D., A.L.Bredemeyer, M.S.D.; Funding

871 Acquisition, M.J.G, K.L., M.S.D; Supervision, M.S.D., M.J.G, C-Y.L., K.L.

872

873 **References:**

874

- 875 1. Madjid, M., Safavi-Naeini, P., Solomon, S. D. & Vardeny, O. Potential Effects of
876 Coronaviruses on the Cardiovascular System: A Review. *JAMA Cardiol.* (2020)
877 doi:10.1001/jamacardio.2020.1286.
- 878 2. Zhou, F. *et al.* Clinical course and risk factors for mortality of adult inpatients with COVID-19
879 in Wuhan, China: a retrospective cohort study. *Lancet Lond. Engl.* **395**, 1054–1062 (2020).
- 880 3. Shi, S. *et al.* Association of Cardiac Injury With Mortality in Hospitalized Patients With
881 COVID-19 in Wuhan, China. *JAMA Cardiol.* (2020) doi:10.1001/jamacardio.2020.0950.
- 882 4. Bhatla, A. *et al.* COVID-19 and Cardiac Arrhythmias. *Heart Rhythm* (2020)
883 doi:10.1016/j.hrthm.2020.06.016.
- 884 5. Huang, L. *et al.* Cardiac Involvement in Patients Recovered From COVID-2019 Identified
885 Using Magnetic Resonance Imaging. *JACC Cardiovasc. Imaging* (2020)
886 doi:10.1016/j.jcmg.2020.05.004.
- 887 6. Puntmann, V. O. *et al.* Outcomes of Cardiovascular Magnetic Resonance Imaging in
888 Patients Recently Recovered From Coronavirus Disease 2019 (COVID-19). *JAMA Cardiol.*
889 (2020) doi:10.1001/jamacardio.2020.3557.
- 890 7. Rajpal, S. *et al.* Cardiovascular Magnetic Resonance Findings in Competitive Athletes
891 Recovering From COVID-19 Infection. *JAMA Cardiol.* (2020)
892 doi:10.1001/jamacardio.2020.4916.
- 893 8. Tersalvi, G. *et al.* Elevated Troponin in Patients With Coronavirus Disease 2019: Possible
894 Mechanisms. *J. Card. Fail.* **26**, 470–475 (2020).
- 895 9. Cleary, S. J. *et al.* Animal models of mechanisms of SARS-CoV-2 infection and COVID-19
896 pathology. *Br. J. Pharmacol.* (2020) doi:10.1111/bph.15143.
- 897 10. Letko, M., Marzi, A. & Munster, V. Functional assessment of cell entry and receptor usage
898 for SARS-CoV-2 and other lineage B betacoronaviruses. *Nat. Microbiol.* **5**, 562–569 (2020).

- 899 11. Wan, Y., Shang, J., Graham, R., Baric, R. S. & Li, F. Receptor Recognition by the Novel
900 Coronavirus from Wuhan: an Analysis Based on Decade-Long Structural Studies of SARS
901 Coronavirus. *J. Virol.* **94**, (2020).
- 902 12. Greenberg, M. J., Daily, N. J., Wang, A., Conway, M. K. & Wakatsuki, T. Genetic and Tissue
903 Engineering Approaches to Modeling the Mechanics of Human Heart Failure for Drug
904 Discovery. *Front. Cardiovasc. Med.* **5**, 120 (2018).
- 905 13. Weinberger, F., Mannhardt, I. & Eschenhagen, T. Engineering Cardiac Muscle Tissue: A
906 Maturing Field of Research. *Circ. Res.* **120**, 1487–1500 (2017).
- 907 14. Karbassi, E. *et al.* Cardiomyocyte maturation: advances in knowledge and implications for
908 regenerative medicine. *Nat. Rev. Cardiol.* **17**, 341–359 (2020).
- 909 15. Hoffmann, M. *et al.* SARS-CoV-2 Cell Entry Depends on ACE2 and TMPRSS2 and Is
910 Blocked by a Clinically Proven Protease Inhibitor. *Cell* **181**, 271-280.e8 (2020).
- 911 16. Bao, L. *et al.* The pathogenicity of SARS-CoV-2 in hACE2 transgenic mice. *Nature* (2020)
912 doi:10.1038/s41586-020-2312-y.
- 913 17. Chen, L., Li, X., Chen, M., Feng, Y. & Xiong, C. The ACE2 expression in human heart
914 indicates new potential mechanism of heart injury among patients infected with SARS-CoV-
915 2. *Cardiovasc. Res.* **116**, 1097–1100 (2020).
- 916 18. Xie, X. *et al.* An Infectious cDNA Clone of SARS-CoV-2. *Cell Host Microbe* **27**, 841-848.e3
917 (2020).
- 918 19. Goldsmith, C. S. *et al.* Ultrastructural characterization of SARS coronavirus. *Emerg. Infect.*
919 *Dis.* **10**, 320–326 (2004).
- 920 20. Goldsmith, C. S., Miller, S. E., Martines, R. B., Bullock, H. A. & Zaki, S. R. Electron
921 microscopy of SARS-CoV-2: a challenging task. *Lancet Lond. Engl.* **395**, e99 (2020).
- 922 21. Kim, D. *et al.* The Architecture of SARS-CoV-2 Transcriptome. *Cell* **181**, 914-921.e10
923 (2020).

- 924 22. Gordon, C. J. *et al.* Remdesivir is a direct-acting antiviral that inhibits RNA-dependent RNA
925 polymerase from severe acute respiratory syndrome coronavirus 2 with high potency. *J.*
926 *Biol. Chem.* **295**, 6785–6797 (2020).
- 927 23. Yin, W. *et al.* Structural basis for inhibition of the RNA-dependent RNA polymerase from
928 SARS-CoV-2 by remdesivir. *Science* **368**, 1499–1504 (2020).
- 929 24. Agostini, M. L. *et al.* Coronavirus Susceptibility to the Antiviral Remdesivir (GS-5734) Is
930 Mediated by the Viral Polymerase and the Proofreading Exoribonuclease. *mBio* **9**, (2018).
- 931 25. Simmons, G., Zmora, P., Gierer, S., Heurich, A. & Pöhlmann, S. Proteolytic activation of the
932 SARS-coronavirus spike protein: cutting enzymes at the cutting edge of antiviral research.
933 *Antiviral Res.* **100**, 605–614 (2013).
- 934 26. Cooper, L. T. Myocarditis. *N. Engl. J. Med.* **360**, 1526–1538 (2009).
- 935 27. Leone, O., Pieroni, M., Rapezzi, C. & Olivetto, I. The spectrum of myocarditis: from
936 pathology to the clinics. *Virchows Arch. Int. J. Pathol.* **475**, 279–301 (2019).
- 937 28. Hu, H., Ma, F., Wei, X. & Fang, Y. Coronavirus fulminant myocarditis saved with
938 glucocorticoid and human immunoglobulin. *Eur. Heart J.* (2020)
939 doi:10.1093/eurheartj/ehaa190.
- 940 29. Zhou, R., Zhang, Q. & Xu, P. TBK1, a central kinase in innate immune sensing of nucleic
941 acids and beyond. *Acta Biochim. Biophys. Sin.* **52**, 757–767 (2020).
- 942 30. Bartok, E. & Hartmann, G. Immune Sensing Mechanisms that Discriminate Self from Altered
943 Self and Foreign Nucleic Acids. *Immunity* **53**, 54–77 (2020).
- 944 31. Michaud, K. *et al.* Diagnosis of myocardial infarction at autopsy: AECVP reappraisal in the
945 light of the current clinical classification. *Virchows Arch. Int. J. Pathol.* **476**, 179–194 (2020).
- 946 32. Sabatasso, S. *et al.* Early markers for myocardial ischemia and sudden cardiac death. *Int. J.*
947 *Legal Med.* **130**, 1265–1280 (2016).
- 948 33. Aljakna, A. *et al.* Multiplex quantitative imaging of human myocardial infarction by mass
949 spectrometry-immunohistochemistry. *Int. J. Legal Med.* **132**, 1675–1684 (2018).

- 950 34. Bojkova, D. *et al.* SARS-CoV-2 infects and induces cytotoxic effects in human
951 cardiomyocytes. *Cardiovasc. Res.* (2020) doi:10.1093/cvr/cvaa267.
- 952 35. Tavazzi, G. *et al.* Myocardial localization of coronavirus in COVID-19 cardiogenic shock.
953 *Eur. J. Heart Fail.* **22**, 911–915 (2020).
- 954 36. Puelles, V. G. *et al.* Multiorgan and Renal Tropism of SARS-CoV-2. *N. Engl. J. Med.* (2020)
955 doi:10.1056/NEJMc2011400.
- 956 37. Lindner, D. *et al.* Association of Cardiac Infection With SARS-CoV-2 in Confirmed COVID-
957 19 Autopsy Cases. *JAMA Cardiol.* (2020) doi:10.1001/jamacardio.2020.3551.
- 958 38. Lamers, M. M. *et al.* SARS-CoV-2 productively infects human gut enterocytes. *Science*
959 (2020) doi:10.1126/science.abc1669.
- 960 39. Monteil, V. *et al.* Inhibition of SARS-CoV-2 Infections in Engineered Human Tissues Using
961 Clinical-Grade Soluble Human ACE2. *Cell* **181**, 905-913.e7 (2020).
- 962 40. Yang, L. *et al.* A Human Pluripotent Stem Cell-based Platform to Study SARS-CoV-2
963 Tropism and Model Virus Infection in Human Cells and Organoids. *Cell Stem Cell* **27**, 125-
964 136.e7 (2020).
- 965 41. Bos, J. M. *et al.* Marked Up-Regulation of ACE2 in Hearts of Patients With Obstructive
966 Hypertrophic Cardiomyopathy: Implications for SARS-CoV-2-Mediated COVID-19. *Mayo*
967 *Clin. Proc.* **95**, 1354–1368 (2020).
- 968 42. Crackower, M. A. *et al.* Angiotensin-converting enzyme 2 is an essential regulator of heart
969 function. *Nature* **417**, 822–828 (2002).
- 970 43. Hinson, J. T. *et al.* HEART DISEASE. Titin mutations in iPS cells define sarcomere
971 insufficiency as a cause of dilated cardiomyopathy. *Science* **349**, 982–986 (2015).
- 972 44. Wijnker, P. J. M. *et al.* Comparison of the effects of a truncating and a missense MYBPC3
973 mutation on contractile parameters of engineered heart tissue. *J. Mol. Cell. Cardiol.* **97**, 82–
974 92 (2016).

- 975 45. Zhang, H. *et al.* Generation of Quiescent Cardiac Fibroblasts From Human Induced
976 Pluripotent Stem Cells for In Vitro Modeling of Cardiac Fibrosis. *Circ. Res.* **125**, 552–566
977 (2019).
- 978 46. Lian, X. *et al.* Efficient differentiation of human pluripotent stem cells to endothelial
979 progenitors via small-molecule activation of WNT signaling. *Stem Cell Rep.* **3**, 804–816
980 (2014).
- 981 47. Dutsch, A. *et al.* Phosphomimetic cardiac myosin-binding protein C partially rescues a
982 cardiomyopathy phenotype in murine engineered heart tissue. *Sci. Rep.* **9**, 18152 (2019).
- 983 48. Truitt, R. *et al.* Increased Afterload Augments Sunitinib-Induced Cardiotoxicity in an
984 Engineered Cardiac Microtissue Model. *JACC Basic Transl. Sci.* **3**, 265–276 (2018).
- 985 49. Zang, R. *et al.* TMPRSS2 and TMPRSS4 promote SARS-CoV-2 infection of human small
986 intestinal enterocytes. *Sci. Immunol.* **5**, (2020).
- 987 50. Zhou, J. *et al.* Infection of bat and human intestinal organoids by SARS-CoV-2. *Nat. Med.*
988 (2020) doi:10.1038/s41591-020-0912-6.
- 989 51. Pipelines, D. *et al.* COVID-19 ARTIC v3 Illumina library construction and sequencing
990 protocol v4 (protocols.io.bgxjxkn). doi:10.17504/protocols.io.bgxjxkn.
- 991 52. ter Meulen, J. *et al.* Human monoclonal antibody combination against SARS coronavirus:
992 synergy and coverage of escape mutants. *PLoS Med.* **3**, e237 (2006).
- 993 53. Case, J. B., Bailey, A. L., Kim, A. S., Chen, R. E. & Diamond, M. S. Growth, detection,
994 quantification, and inactivation of SARS-CoV-2. *Virology* **548**, 39–48 (2020).
- 995 54. Love, M. I., Huber, W. & Anders, S. Moderated estimation of fold change and dispersion for
996 RNA-seq data with DESeq2. *Genome Biol.* **15**, 550 (2014).
- 997 55. Meder, B. *et al.* Epigenome-Wide Association Study Identifies Cardiac Gene Patterning and
998 a Novel Class of Biomarkers for Heart Failure. *Circulation* **136**, 1528–1544 (2017).

- 999 56. Clippinger, S. R. *et al.* Disrupted mechanobiology links the molecular and cellular
1000 phenotypes in familial dilated cardiomyopathy. *Proc. Natl. Acad. Sci. U. S. A.* **116**, 17831–
1001 17840 (2019).
- 1002 57. Lian, X. *et al.* Robust cardiomyocyte differentiation from human pluripotent stem cells via
1003 temporal modulation of canonical Wnt signaling. *Proc. Natl. Acad. Sci. U. S. A.* **109**, E1848–
1004 1857 (2012).
- 1005 58. Lian, X. *et al.* Directed cardiomyocyte differentiation from human pluripotent stem cells by
1006 modulating Wnt/ β -catenin signaling under fully defined conditions. *Nat. Protoc.* **8**, 162–175
1007 (2013).
- 1008 59. Sharma, A. *et al.* Derivation of highly purified cardiomyocytes from human induced
1009 pluripotent stem cells using small molecule-modulated differentiation and subsequent
1010 glucose starvation. *J. Vis. Exp. JoVE* (2015) doi:10.3791/52628.
- 1011 60. Dege, C. & Sturgeon, C. M. Directed Differentiation of Primitive and Definitive
1012 Hematopoietic Progenitors from Human Pluripotent Stem Cells. *J. Vis. Exp. JoVE* (2017)
1013 doi:10.3791/55196.
- 1014 61. Schindelin, J. *et al.* Fiji: an open-source platform for biological-image analysis. *Nat. Methods*
1015 **9**, 676–682 (2012).
- 1016 62. Breckwoldt, K. *et al.* Differentiation of cardiomyocytes and generation of human engineered
1017 heart tissue. *Nat. Protoc.* **12**, 1177–1197 (2017).
- 1018 63. Dobin, A. *et al.* STAR: ultrafast universal RNA-seq aligner. *Bioinforma. Oxf. Engl.* **29**, 15–21
1019 (2013).
- 1020 64. Liao, Y., Smyth, G. K. & Shi, W. featureCounts: an efficient general purpose program for
1021 assigning sequence reads to genomic features. *Bioinforma. Oxf. Engl.* **30**, 923–930 (2014).
- 1022 65. Patro, R., Duggal, G., Love, M. I., Irizarry, R. A. & Kingsford, C. Salmon provides fast and
1023 bias-aware quantification of transcript expression. *Nat. Methods* **14**, 417–419 (2017).

- 1024 66. Wang, L., Wang, S. & Li, W. RSeQC: quality control of RNA-seq experiments. *Bioinforma.*
1025 *Oxf. Engl.* **28**, 2184–2185 (2012).
- 1026 67. Robinson, M. D., McCarthy, D. J. & Smyth, G. K. edgeR: a Bioconductor package for
1027 differential expression analysis of digital gene expression data. *Bioinforma. Oxf. Engl.* **26**,
1028 139–140 (2010).
- 1029 68. Ritchie, M. E. *et al.* limma powers differential expression analyses for RNA-sequencing and
1030 microarray studies. *Nucleic Acids Res.* **43**, e47 (2015).
- 1031 69. Liu, R. *et al.* Why weight? Modelling sample and observational level variability improves
1032 power in RNA-seq analyses. *Nucleic Acids Res.* **43**, e97 (2015).
- 1033 70. Luo, W., Friedman, M. S., Shedden, K., Hankenson, K. D. & Woolf, P. J. GAGE: generally
1034 applicable gene set enrichment for pathway analysis. *BMC Bioinformatics* **10**, 161 (2009).
- 1035 71. Zhao, S., Guo, Y., Sheng, Q. & Shyr, Y. Advanced heat map and clustering analysis using
1036 heatmap3. *BioMed Res. Int.* **2014**, 986048 (2014).
- 1037 72. Luo, W. & Brouwer, C. Pathview: an R/Bioconductor package for pathway-based data
1038 integration and visualization. *Bioinforma. Oxf. Engl.* **29**, 1830–1831 (2013).
- 1039 73. Langfelder, P. & Horvath, S. WGCNA: an R package for weighted correlation network
1040 analysis. *BMC Bioinformatics* **9**, 559 (2008).
- 1041 74. Yu, G., Wang, L.-G., Han, Y. & He, Q.-Y. clusterProfiler: an R package for comparing
1042 biological themes among gene clusters. *Omics J. Integr. Biol.* **16**, 284–287 (2012).
- 1043
1044

1045 **Key Resources Table:**

REAGENT or RESOURCE	SOURCE	IDENTIFIER
Antibodies		
Anti-CoV spike	PMID: 16796401	CR3022
Anti-human CD14 APC	Biolegend	RRID: AB_314190
Anti-human CD68	BioRad	RRID: AB_2074721
Anti-human Sarcomeric actin	Sigma	Clone: A2127
Anti-human ACE2	Abcam	RRID: AB_301861
Anti-human Ki67	Abcam	RRID: AB_302459
Anti-SARS-CoV-2 nucleocapsid protein	Sino Biological	RRID: AB_2827974
Anti-TNNT2	Miltenyi Biotech	RRID: AB_2783891
Anti-human CCR2	Abcam	Cat# ab176390
Anti-rabbit TNNT2	Abcam	Cat# ab45932
Cy3 donkey anti-rabbit	Jackson Immunoresearch	Cat# 711165152
Anti-human TNNT2	ThermoFisher	Cat# MS-295-P0
Anti-human CD14 PE	Biolegend	RRID: AB_314188
Anti-human CD64 PE-Cy7	Biolegend	RRID: AB_2561584
Anti-human CD45 FITC	Biolegend	RRID: AB_314394
Anti-human CD31 BV421	Biolegend	RRID: AB_2563810

Anti-human CD90 PE	Biolegend	RRID: AB_893433
Anti-human CD34 PE-Cy7	BD Biosciences	Cat # 560710
Anti-human CD184 APC	BD Biosciences	Cat #560936
Anti-human CD73 PE	BD Biosciences	Cat #550257
Bacterial and Virus Strains		
SARS-CoV-2	CDC	2019n-CoV/USA_WA1/2019
SARS-CoV-2_mNeonGreen	PY Shi	PMID: 32289263
Chemicals, Peptides, and Recombinant Proteins		
Camostat Mesilate	Selleckchem	S2874
E-64	Selleckchem	S7379
Remdesivir		
SB431542	Tocris	1614
M-CSF	R&D Systems	Cat # 216-MC
VEGF	R&D Systems	Cat # 293-VE
Critical Commercial Assays		
Opal 4-Color Manual IHC Kit	Perkin-Elmer	Cat# NEL810001KT
<i>In Situ</i> Cell Death Detection Kit	Roche	Cat# 12156792910

RNAscope 2.5 HD Detection Reagent – RED	Advanced Cell Diagnostics	Cat# 322360
RNAscope Multiplex Fluorescent Reagent Kit v2 Assay	Advanced Cell Diagnostics	Cat# 323100
Experimental Models: Cell Lines		
human BJ fibroblast cells	ATCC	Cat#CRL-2522
human induced pluripotent stem cell line	Genome Engineering and iPSC Center at Washington University	Cat#BJFF.6
Experimental Models: Organisms/Strains		
Oligonucleotides		
F: ATGCTGCAATCGTGCTACAA	IDT	PMC7293183
R: GACTGCCGCCTCTGCTC	IDT	PMC7293183
P: 56-FAM/TCAAGGAAC/ZEN/AACATTGCCAA/3IABkFQ/	IDT	PMC7293183
Primers for B2M, ACE2, TMPRSS2, MYH7, TNNT2, OAS1, MX1 in table S1	IDT	N/A
Software and Algorithms		
MATLAB	Mathworks	Version 2020a
Other		
Dow SYLGARD™ 184 Silicone Encapsulant Clear 0.5 kg Kit	Ellsworth Adhesives	Cat#184 SIL ELAST KIT 0.5KG
Collagen I, Rat Tail	Corning	Cat#354236

Y-27632	Selleck Chemicals	Cat#S1049
Teflon spacer	EHT Technologies GmbH	Cat#C0002
Silicone rack	EHT Technologies GmbH	Cat#C0001
Pluronic F-127	ThermoFisher	Cat#P6866
Growth Factor Reduced Matrigel	Corning	Cat#354230
Fetal bovine serum (FBS)	MilliporeSigma	Cat#F0926

1046

1047

1048

1049

1050

1051

1052

1053 Table S1. Primers for qPCR-base evaluation of human host gene expression

Gene	Forward (5'-3')	Reverse (5'-3')
ACE2	GAGAAGTGGAGGTGGATGG	ACATGGAACAGAGATGCGG
TMPRSS2	GGAGTGTACGGGAATGTGATG	CCAGCCCCATTGTTTTCTTG
B2M	TGCTGTCTCCATGTTTGATGTATCT	TCTCTGCTCCCCACCTCTAAGT
TNNT2	AGCGGAAAAGTGGGAAGAG	TCCAAGTTATAGATGCTCTGCC
Oas1	CATCTGTGGGTTCTGAAGG	GAGAGGACTGAGGAAGACAAC
Mx1	GAAGATAAGTGGAGAGGCAAGG	CTCCAGGGTGATTAGCTCATG
TNF	ACTTTGGAGTGATCGGCC	GCTTGAGGGTTTGCTACAAC
MYH7	CATTGACTTTGGCATGGACC	CAAACAGCTTGGCCTTGAAG

1054

1055

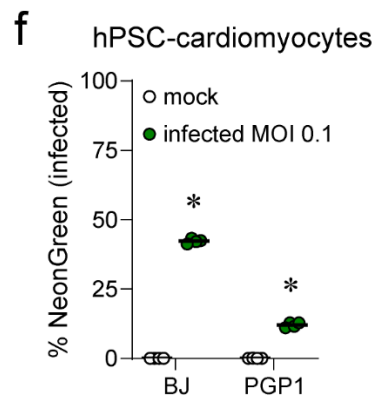
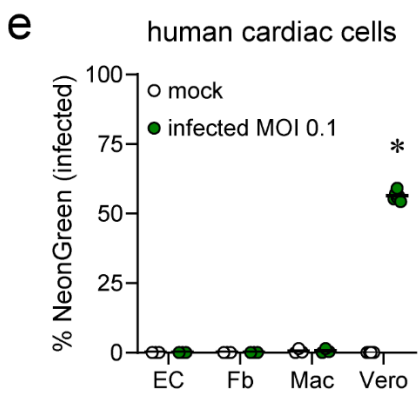
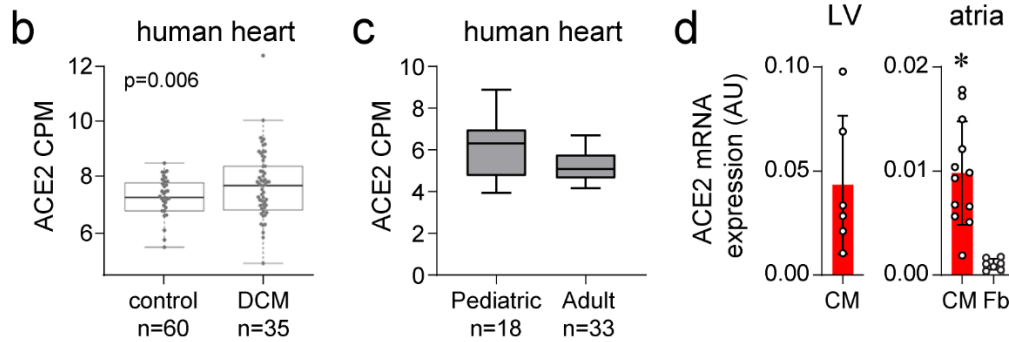
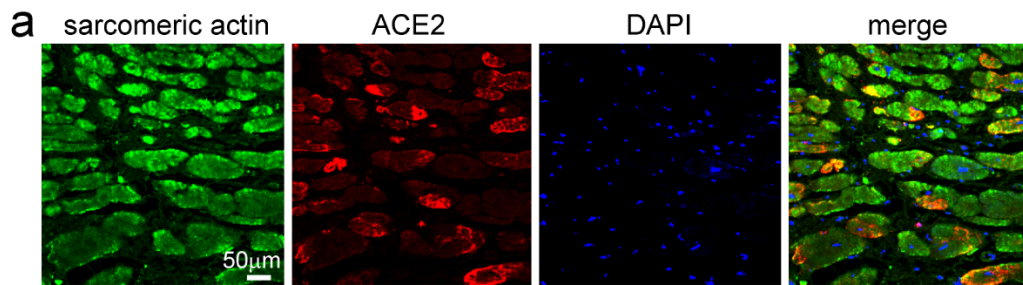


Figure 1: ACE2 is expressed in the human heart and in stem cell derived cardiomyocytes.

a, Immunohistochemistry of human heart tissue showing ACE2 (red) expression in cardiomyocytes (green, sarcomeric actin). Representative images from 5 analyzed specimens. **b**, RNA sequencing demonstrating ACE2 mRNA expression in myocardial biopsies obtained from adult controls and heart failure patients. Data is displayed as counts per million (CPM). n=18 pediatric, n=33 adult. Each data point indicates an individual sample. n=60 controls, n=35 heart failure. **c**, RNA sequencing demonstrating ACE2 mRNA expression in adult and pediatric heart tissue. Data is displayed as counts per million (CPM). n=18 pediatric, n=33 adult. **d**, Quantitative RT-PCR measurements showing ACE2 mRNA expression in human primary left ventricular (LV), cardiomyocytes (CM), atrial cardiomyocytes, and atrial fibroblasts (Fb). Each data point indicates an individual sample. Error bars denote standard deviation. * p<0.05 compared to atrial fibroblasts (Mann-Whitney test). **e**, Inoculation of primary human endothelial cells (EC), fibroblasts (Fb), and macrophages (Mac) with mock (black) or SARS2-CoV-2-NeonGreen (green, MOI 0.1). Vero cells are included as a positive control. Data is presented as the percent of live cells that express NeonGreen indicating infection. Each data point represents cells isolated from an individual patient sample. Bars denote mean values. * p<0.05 compared to mock infection (Mann-Whitney test). **f**, Inoculation of 2 different hPSC-derived cardiomyocyte lines (BJ, PGP1) with mock (black) or SARS2-CoV-2-NeonGreen (green, MOI 0.1, 1.0). Each data point represents biological replicates. * p<0.05 compared to mock infection (Mann-Whitney test). Bars denote mean values.

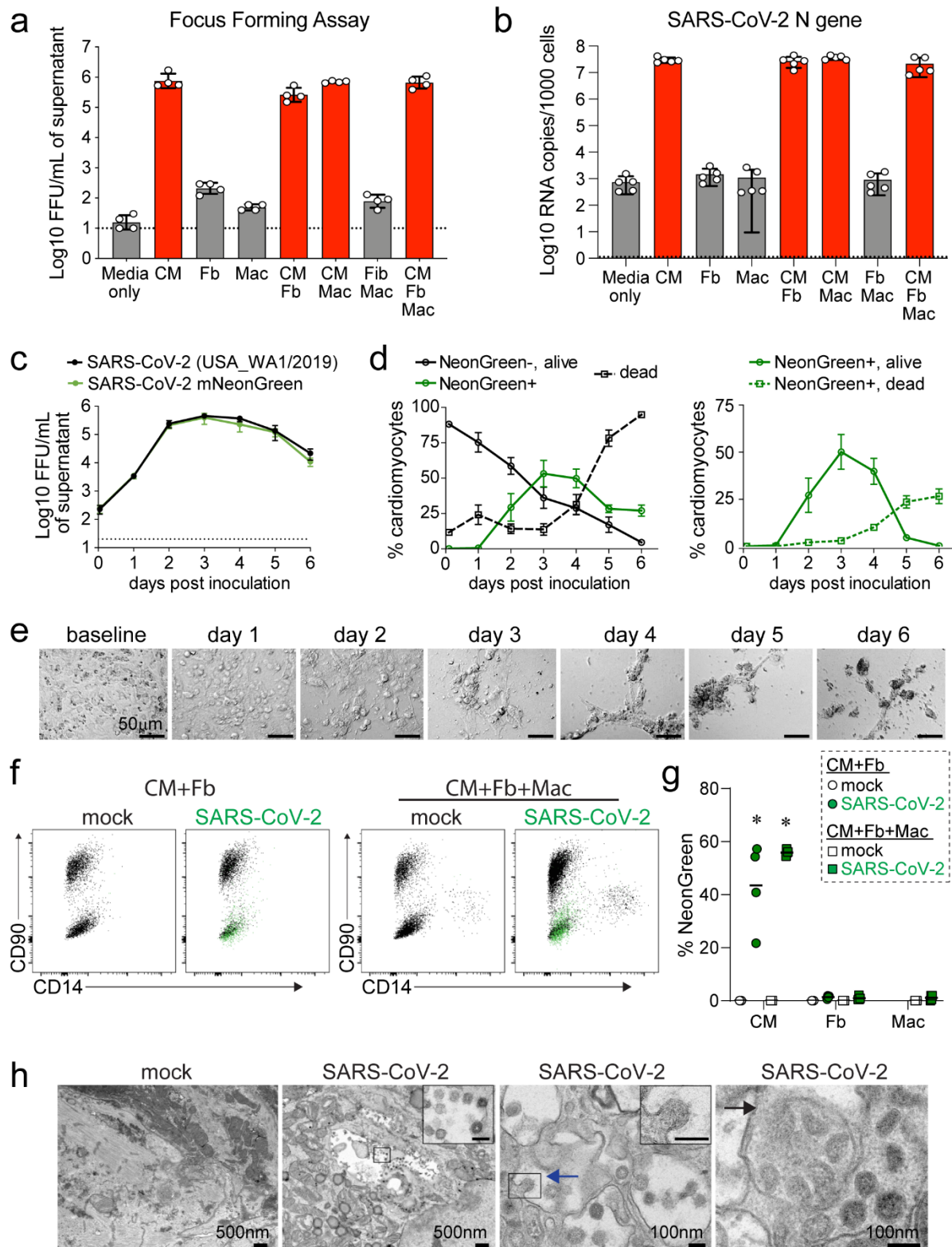


Figure 2: SARS-CoV-2 infects cardiomyocytes. **a**, Focus forming assay demonstrating production of infectious virus from cultures containing hPSC-derived cardiomyocytes (CM), fibroblasts (Fb), and macrophages (Mac) inoculated with SARS-CoV-2 (MOI 0.1). Media only denotes wells that contain no cells. Assays were performed 3 days following inoculation. Dashed line shows the limit of assay detection. **b**, Quantitative RT-PCR showing viral N gene copies in cultures containing CM, Fb, and Macs inoculated with SARS-CoV-2 (MOI 0.1). RNA was collected 3 days after inoculation. Data points indicate individual samples (n=5, a-b). Bars denote the mean value and error bars indicate standard error of the mean. **c**, Focus forming assay measuring infectious SARS-CoV-2 (wild-type, black; mNeonGreen, green) in supernatant of hPSC-derived cardiomyocytes over time following inoculation (MOI 0.1). Dashed line shows the limit of detection. n=4 per experimental group. Error bars denote standard deviation. **d**, Two-dimensional cultures of hPSC-derived cardiomyocytes were inoculated with SARS-CoV-2 (MOI 0.1) and analyzed for viability (Zombie-Violet) and infection (NeonGreen reporter) as a function of time by flow cytometry. Right plot: viability of NeonGreen positive cells. n=4 per experimental group. Error bars denote standard deviation. **e**, Brightfield microscopy showing cytopathic effect (CPE) in hPSC-derived cardiomyocytes infected with SARS-CoV-2 (MOI 0.1). Representative images from 5 individual samples. **f**, Flow cytometry of two-dimensional tissues containing CM and Fb (left) or CM, Fb, and Mac (right) harvested on day 3 following either mock infection or inoculation with SARS-CoV-2 (MOI 0.1). Representative plot from 4 independent samples. Cardiomyocytes (CD90-CD14-) demonstrated prominent NeonGreen fluorescence (green overlay). NeonGreen signal was not detected in fibroblasts (CD90+CD14-) or macrophages (CD90-CD14+). **g**, Quantification of the percent NeonGreen positive cells from 2-dimensional tissues containing hPSC-CMs and fibroblasts or hPSC-CMs, fibroblasts, and macrophages. Data points indicate individual samples (n=4). * p<0.05 compared to mock infection (Mann-Whitney test). **h**, Transmission electron microscopy micrographs of cardiomyocytes in two-dimensional tissues infected with either mock or SARS-CoV-2 (MOI 0.1). Tissues were harvested on day 3 post-inoculation. Virions are readily apparent. Viral budding (blue arrow) and endosomal compartments filled with virions (black arrow) are denoted. Scale bars in insets are 100 nm. Representative image from 4 independent samples.

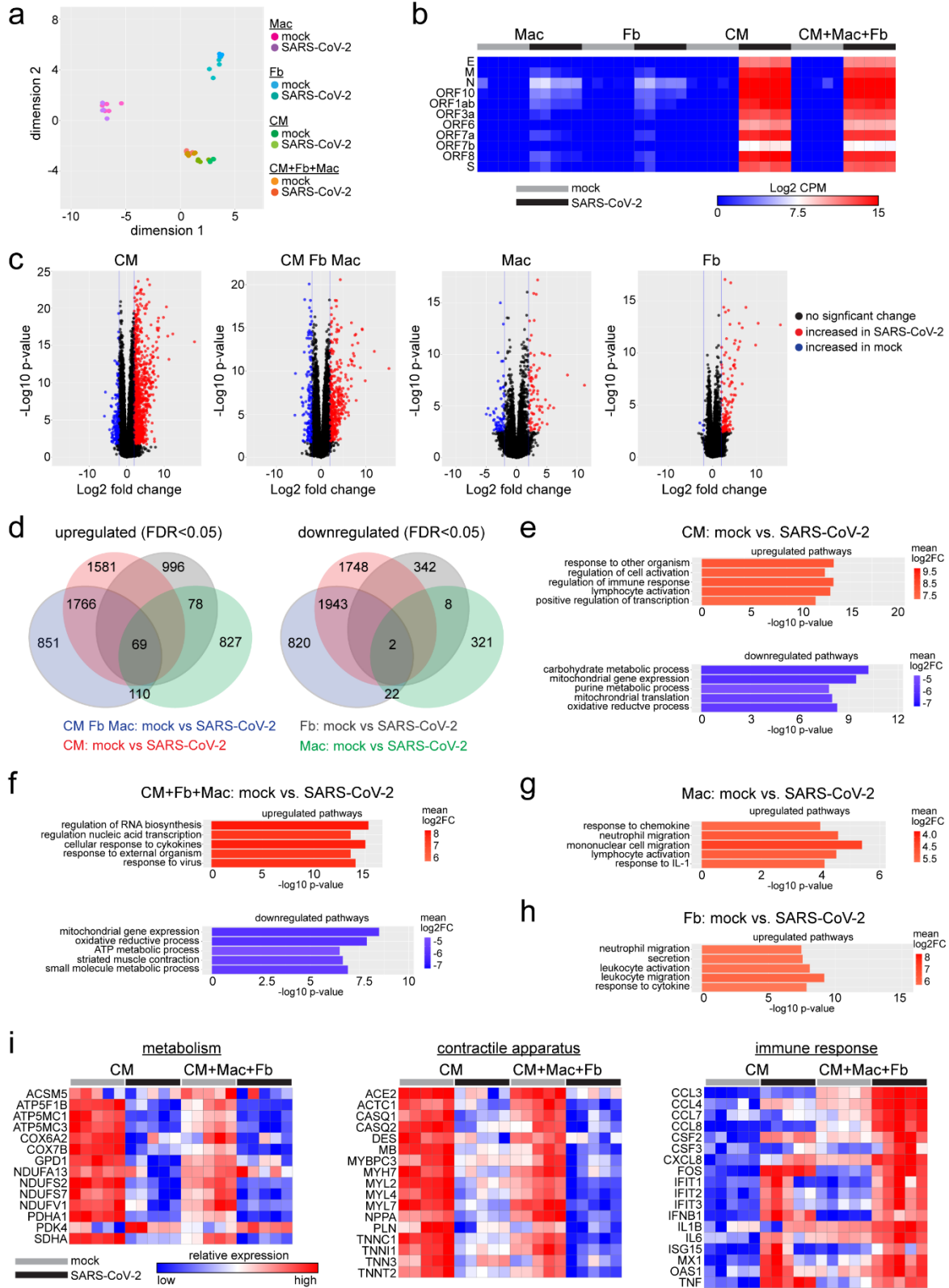


Figure 3: RNA sequencing identified robust viral transcription and activation of innate immune response in hPSC-derived cardiomyocytes and 2D tissues. **a**, MDS plot of RNA sequencing data obtained from mock and SARS-CoV-2 infected (MOI 0.1) hPSC-derived cardiomyocytes (CM), fibroblasts (Fb), macrophages (Mac), and two-dimensional tissues (CM+Fb+Mac) containing all 3 cellular components. Cells and tissues were harvested on day 3 post-inoculation. n=5 per experimental group. **b**, Heatmap of SARS-CoV-2 viral gene expression in each condition. Color scale denotes absolute expression as log₂ of counts per million reads (CPM) (blue=0, red=15). **c**, Volcano plots showing differentially expressed genes between mock and SARS-CoV-2 infected conditions. Black: no significant change, Red: upregulated during infection (log₂ fold change>2, FDR p-value<0.05), blue: downregulated during infection (log₂ fold change<2, FDR p-value<0.05). Data points correspond to individual genes or transcripts. **d**, Venn diagram of genes upregulated and downregulated in each cell type and two-dimensional tissues. Differential expression is based on change relative to corresponding uninfected (mock) samples. **e-h**, GO Pathway analysis of CM (**e**), CM+Fb+Mac (**f**), Mac (**g**) and Fib (**h**) showing top five upregulated (red) and downregulated (blue) pathways in SARS-CoV-2-infected samples compared to mock. Color indicates log₂ fold change (log₂FC). **i**, Heat maps of selected differentially expressed genes implicated in metabolism (left), contractile apparatus (center) and immune response (right). CM and two-dimensional tissues (CM+Mac+Fb) are displayed. Color scale denotes relative gene expression (high-red, low-blue) across cell types and conditions.

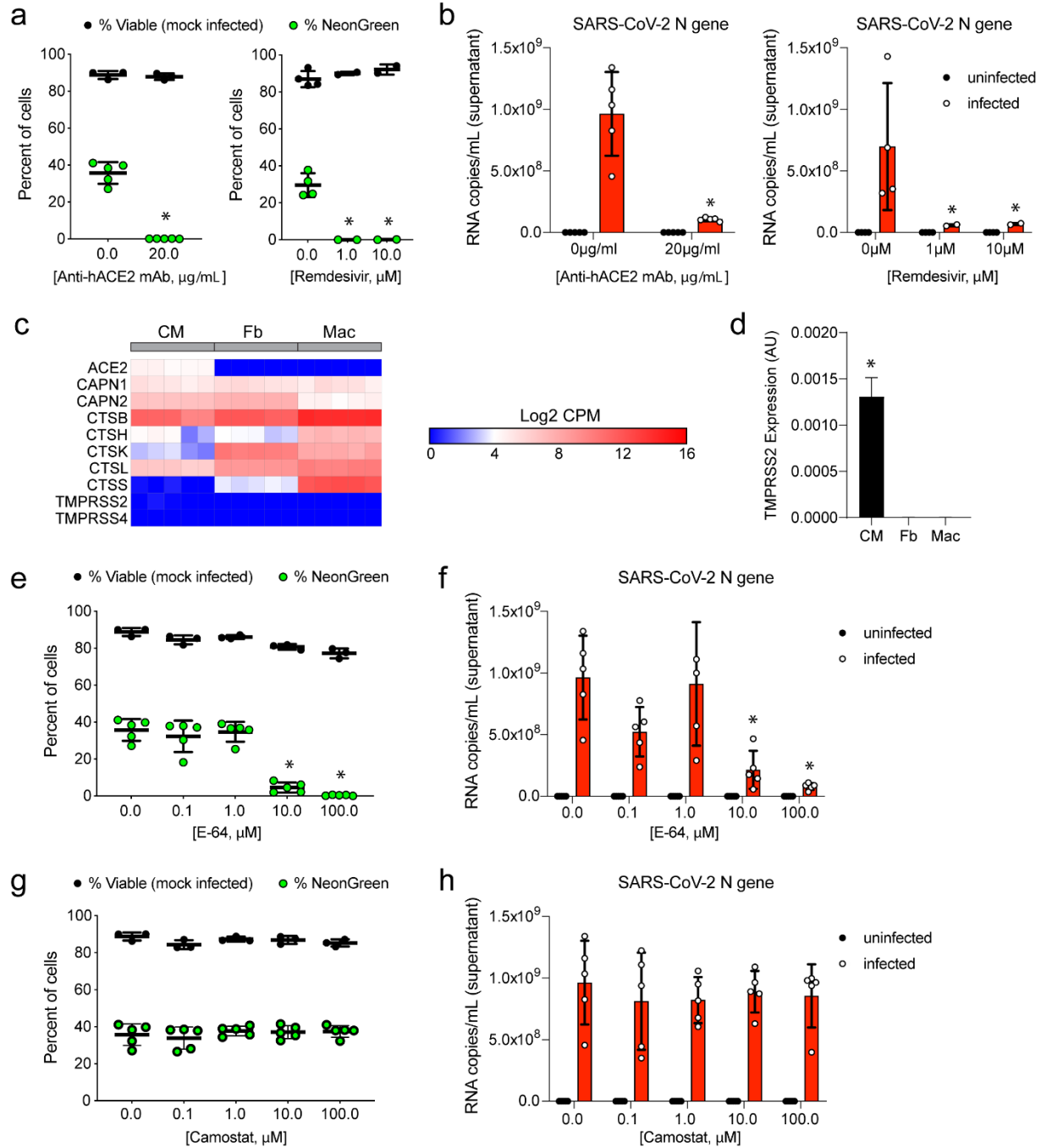


Figure 4. SARS-CoV-2 entry of hPSC-derived cardiomyocytes is mediated by ACE2 and endosomal cysteine proteases. **a-b**, hPSC-derived cardiomyocytes were infected with mock or inoculated with SARS-CoV-2-mNeonGreen (MOI 0.1). Cells were treated with either vehicle control, anti-human ACE2 neutralizing antibody (Anti-hACE2 mAb, left), or remdesivir (inhibitor of RNA-dependent RNA polymerase, right) at the indicated concentrations. Cells were analyzed by flow cytometry on day 3 post-inoculation for viral infection (NeonGreen, green circles) and viability (Zombie-Violet, black circles) (**a**). The presence of viral RNA in the tissue culture supernatant was also quantified by RT-PCR (**b**). Each data point corresponds to an individual sample/experiment, error bars denote standard error of the mean, * $p < 0.05$ compared to infected cells treated with vehicle control (Mann-Whitney test). **c**, Heatmap of host genes implicated in SARS-CoV-2 cell entry in uninfected hPSC-derived cardiomyocytes (CM), fibroblasts (Fb), and macrophages (Mac). Color scale indicates absolute gene expression levels. **d**, Quantitative RT-PCR for *TMPRSS2* in uninfected hPSC-derived cardiomyocytes (CM), fibroblasts (Fb), and macrophages (Mac). $n = 5$ for each cell type, error bars denote standard error of the mean, * $p < 0.05$ compared to other cell populations (Mann-Whitney test). **e-h**, hPSC-derived cardiomyocytes were mock infected or inoculated with SARS-CoV2-mNeonGreen (MOI 0.1). Cells were treated with either vehicle control, endosomal cysteine protease inhibitor E-64 (**e-f**), or serine protease inhibitor camostat (**g-h**) at the indicated concentrations. Cells were analyzed by flow cytometry on day 3 post-inoculation for viral infection (NeonGreen, green circles) and viability (Zombie-Violet, black circles) (**e,g**). Viral RNA in the tissue culture supernatant was quantified by RT-PCR (**f,h**). Each data point corresponds to an individual sample/experiment, error bars denote standard error of the mean, * $p < 0.05$ compared to infected cells treated with vehicle control (Mann-Whitney test).

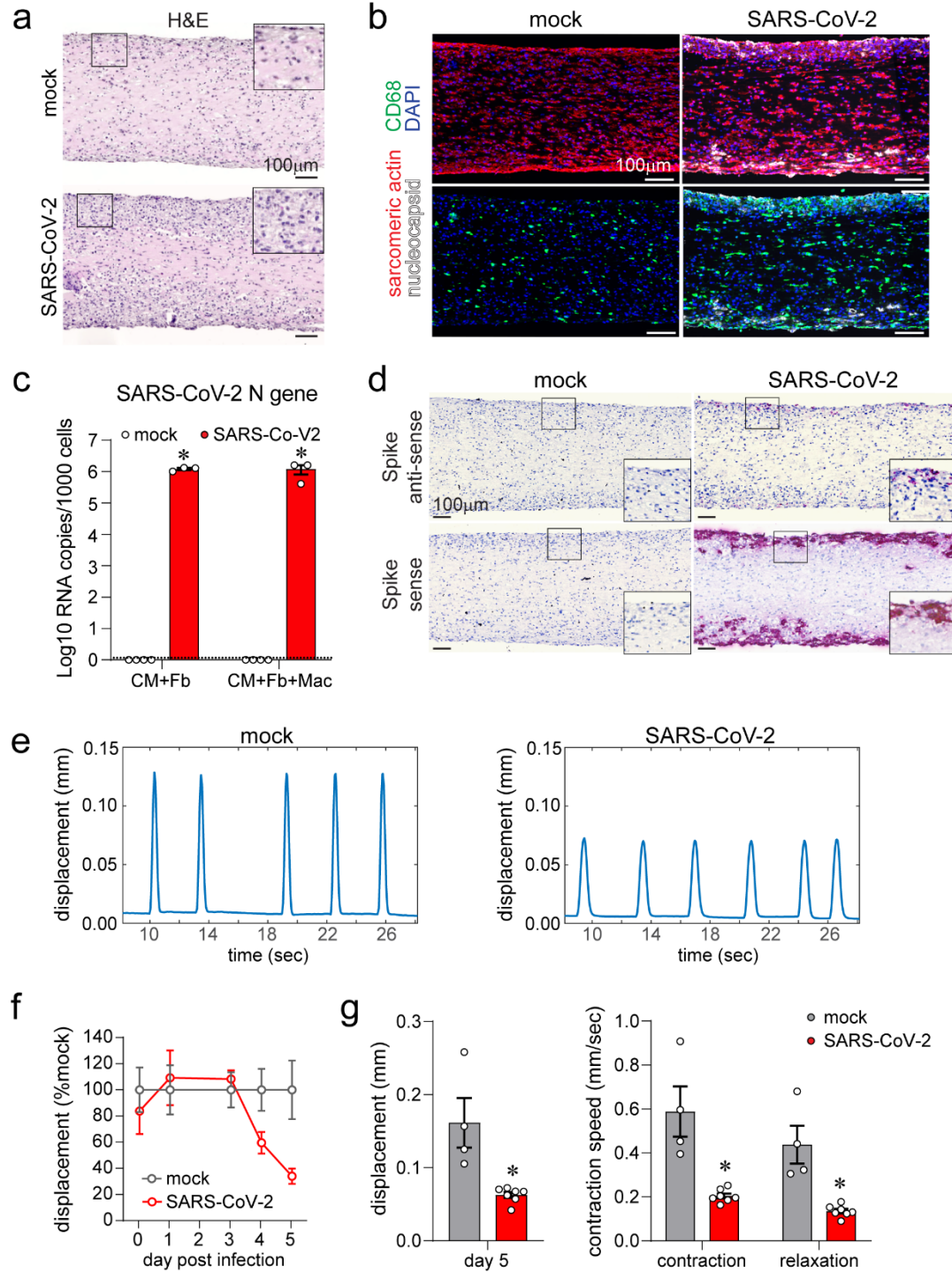


Figure 5. Human engineered heart tissues (EHTs) recapitulate aspects of COVID-19 myocarditis. **a**, Representative hematoxylin and eosin (H&E) stained histology images of three-dimensional EHTs consisting of hPSC-derived cardiomyocytes (CM), fibroblasts (Fb), and macrophages (Macs) 5 days following mock infection or inoculation with SARS-CoV-2 (MOI 0.1). Insets are high magnification images of the boxed areas. Representative images from 4 independent samples. **b**, Immunostaining of mock or SARS-CoV-2 infected three-dimensional EHTs for sarcomeric actin (cardiomyocytes, red), CD68 (macrophages, green), and nucleocapsid protein (white). EHTs were harvested 5 days after inoculation. Blue: DAPI. Images are representative of 4 independent experiments. Representative images from 4 independent samples. **c**, Quantitative RT-PCR of SARS-CoV-2 N gene expression in EHTs consisting of hPSC-derived cardiomyocytes (CM) and fibroblasts (Fb) or hPSC-derived cardiomyocytes, fibroblasts, and macrophages. EHTs were either mock infected or inoculated with SARS-CoV-2 (MOI 0.1) and harvested 5 days after inoculation. Each data point represents individual samples/experiments. Error bars denote standard error of the mean. Bar height represents sample mean. Dotted line: limit of detection. * $p < 0.05$ compared to uninfected control (mock, Mann-Whitney test). **d**, *In situ* hybridization for SARS-CoV-2 ORF1ab RNA sense and anti-sense strands (red) in EHTs 5 days after mock or SARS-CoV-2 infection (MOI 0.1). Hematoxylin: blue. Representative images from 4 independent specimens. Insets are high magnification images of the boxed areas. **e**, Representative spontaneous beating displacement traces for an infected and an uninfected EHT on day 5 post-infection. Videos used to generate these traces can be found in **Supplemental Videos 1 and 2**. **f**, Displacement (relative to uninfected mock condition) generated by spontaneous beating of EHTs as a function of time following inoculation with SARS-CoV-2 (MOI 0.1). Each data point represents a mean value from 4-7 independent samples (2 independent experiments), error bars denote standard error of the mean. **g**, Quantification of absolute displacement (left) and contraction speed (right) generated by spontaneous beating of EHTs 5 days following mock or SARS-CoV-2 infection (MOI 0.1). Each data point denotes an individual EHT, bar height corresponds to mean displacement, error bars represent standard error of the mean, * $p < 0.05$ compared to mock (Mann-Whitney test).

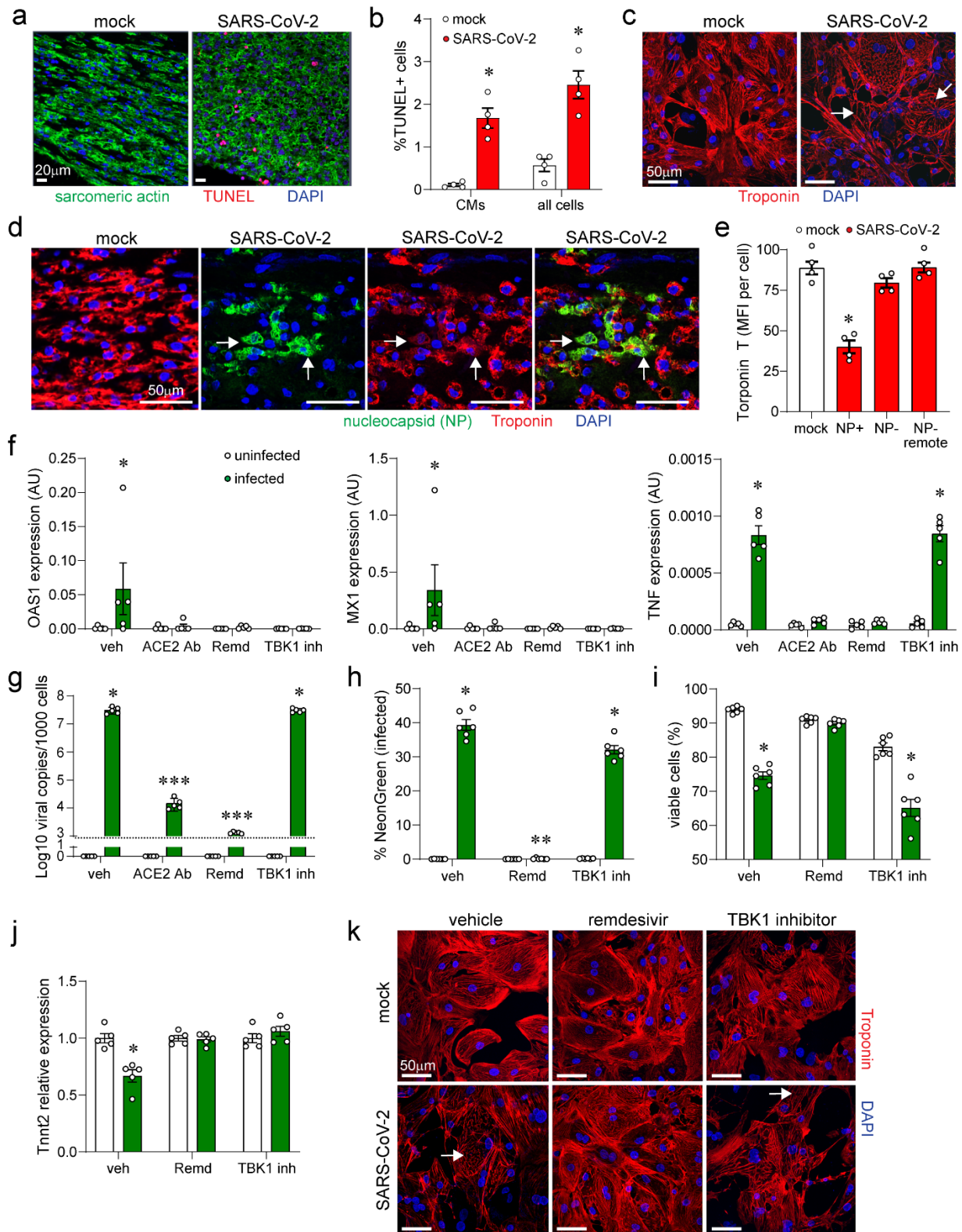


Figure 6. Mechanisms of reduced EHT contractility. **a**, Combined immunostaining for cardiomyocytes (cardiac actin, green) and TUNEL staining (red) of EHTs (CM+Fb+Mac) 5 days after mock or SARS-CoV-2 infection (MOI 0.1). DAPI: blue. Representative images from 4 independent experiments. **b**, Quantification of cell death (percent of TUNEL-positive cells) in areas of viral infection. Each data point denotes an individual EHT, bar height corresponds to the mean, error bars represent standard error of the mean, * $p < 0.05$ compared to mock (Mann-Whitney test). **c**, Immunostaining of hPSC-derived cardiomyocytes for Troponin T (red) 3 days after inoculation with mock control or SARS-CoV-2-NeonGreen (MOI 0.1). Blue: DAPI. Arrows denote areas of sarcomere disassembly. **d**, Immunostaining of EHTs for Troponin T (red) and SARS-CoV-2 nucleocapsid (green) 5 days after inoculation with mock control or SARS-CoV-2-NeonGreen (MOI 0.1). Blue: DAPI. Arrows denote SARS-CoV-2 nucleocapsid positive cells with reduced Troponin T staining. **e**, Quantification of Troponin T staining in mock (white) and SARS-CoV-2 (red) infected EHTs. NP: nucleocapsid. Data is presented as mean fluorescence intensity (MFI). MFI was measured in infected (NP+) cardiomyocytes and uninfected (NP-) cardiomyocytes located proximal or remote to areas of infection. Each data point denotes an individual EHT, bar height corresponds to the mean, error bars represent standard error of the mean, * $p < 0.05$ compared to mock (Mann-Whitney test). **f**, Quantitative RT-PCR measuring OAS1, MX1, and TNF mRNA expression in hPSC-derived cardiomyocytes 3 days after inoculation with mock control (white) or SARS-CoV-2 (green, MOI 0.1). Cells were treated with vehicle, ACE2 antibody (ACE2 Ab) (20 μ g/ml), remdesivir (10 μ M), or TBK inhibitor (MRT67307, 10 μ M). Each data point denotes a biologically unique sample, bar height corresponds to the mean, and error bars indicate standard error of the mean. * $p < 0.05$ compared to mock control. **g**, Quantitative RT-PCR of SARS-CoV-2 N gene expression in hPSC-derived cardiomyocytes that were either mock infected (white) or inoculated with SARS-CoV-2 (green, MOI 0.1) and harvested 3 days after inoculation. Cells were treated with vehicle, ACE2 Ab (20 μ g/ml), remdesivir (10 μ M), or TBK1 inhibitor (MRT67307, 10 μ M). Each data point represents individual samples. Error bars denote standard error of the mean. Bar height represents sample mean. Dotted line: limit of detection. * $p < 0.05$ compared to uninfected control. *** $p < 0.05$ compared to uninfected control and vehicle infected (mock, Mann-Whitney test). **h-i**, Flow cytometry measuring the percent of infected (h) and viable (i) hPSC-derived cardiomyocytes following either mock infection (white) or inoculation with SARS-CoV-2 (green, MOI 0.1). Cells were harvested and analyzed 3 days after inoculation. Cells were treated with vehicle, remdesivir (10 μ M), or TBK1 inhibitor (MRT67307, 10 μ M). Each data point represents individual samples. Error bars denote standard error of the mean. Bar height represents sample mean. * $p < 0.05$ compared to uninfected control. ** $p < 0.05$ compared to vehicle infected (mock, Mann-Whitney test). **j**, Quantitative RT-PCR measuring TNNT2 mRNA expression in hPSC-derived cardiomyocytes 3 days after inoculation with mock control (white) or SARS-CoV-2 (green, MOI 0.1). Cells were treated with vehicle, ACE2 Ab (20 μ g/ml), remdesivir (10 μ M), or TBK inhibitor (MRT67307, 10 μ M). Each data point denotes a biologically unique sample, bar height corresponds to the mean, and error bars indicate standard error of the mean. * $p < 0.05$ compared to mock control. **k**, Immunostaining of hPSC-derived cardiomyocytes for Troponin T (red) 3 days after inoculation with mock control or SARS-CoV-2-NeonGreen (MOI 0.1). hPSC-derived cardiomyocytes were treated with vehicle, remdesivir (10 μ M) or TBK inhibitor (MRT67307, 10 μ M). Blue: DAPI. Arrows denote areas of sarcomere disassembly. Merged images can be found in Fig. S8.

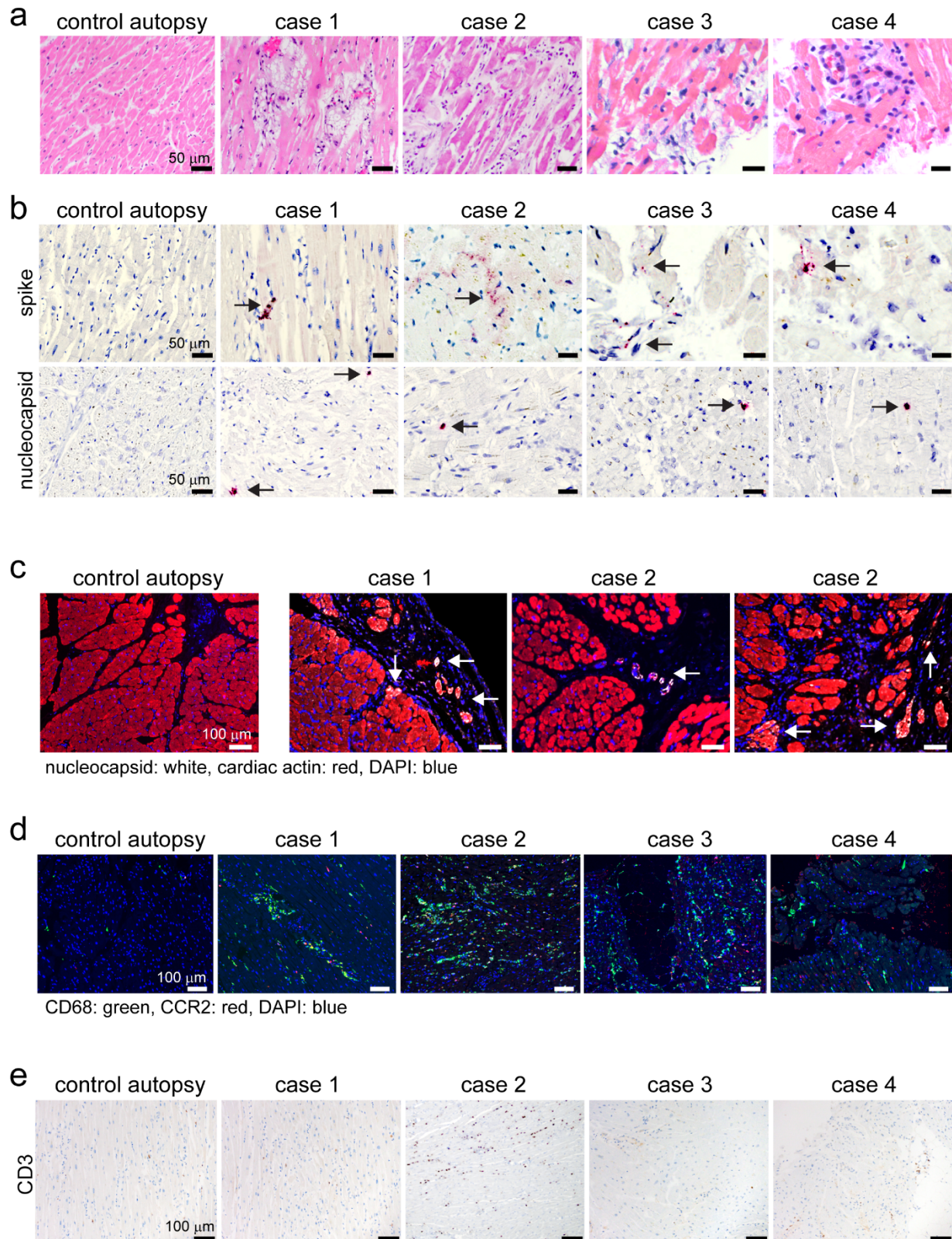


Figure 7. Human autopsy and endomyocardial tissue from patients with suspected COVID-19 myocarditis show evidence of SARS-CoV-2 cardiomyocyte infection. **a**, Hematoxylin and eosin staining of cardiac autopsy (anterior left ventricular wall) and biopsy samples (right ventricular septum) from subjects without COVID-19 (control case) and patients with a clinical diagnosis of COVID-19 myocarditis (case 1-4). **b**, *In situ* hybridization of cardiac autopsy and biopsy tissue for SARS-CoV-2 spike and nucleocapsid RNA (red) showing evidence of viral infection. Hematoxylin: blue. Arrows denotes viral RNA staining in cells with cardiomyocyte morphology. **c**, Immunostaining of control and COVID-19 myocarditis cardiac autopsy tissue for SARS-CoV-2 nucleocapsid (white) and cardiac actin (red). DAPI: blue. Arrows denotes nucleocapsid staining in cardiomyocytes. **d**, Immunostaining of control and COVID-19 myocarditis cardiac autopsy and biopsy tissue for CD68 (green) and CCR2 (red). DAPI: blue. **e**, Immunostaining of control and COVID-19 myocarditis cardiac autopsy and biopsy tissue for CD3 (brown). Hematoxylin: blue.